Chapter 6

Radon Detection and Techniques

"In dreams, we enter a world that's entirely our own."
- Albus Dumbledore

The SuperNEMO requirement for radon in the tracker gas to be less than 0.15 mBq/m^3 poses a significant challenge not only from a technical point of view but also from a measurement point of view. The best commercial radon detectors in the world are only able to achieve sensitivities of 0.1 Bq/m^3. Therefore, for use in the SuperNEMO experiment an electrostatic detector was especially developed with significantly improved sensitivity, however, it was still not able to achieve the necessary sensitivity. A new system therefore had to be developed to further improve sensitivities in order to monitor and confirm the challenging SuperNEMO target had been achieved.

6.1 The Electrostatic Detector

A custom-made electrostatic detector, shown in Figure 6.1a, originally developed for high sensitivity radon measurements for the ELEGANT V and Super-Kamiokande experiments [53, 54] was acquired for SuperNEMO. It is capable of measuring radon activities to 1-2 mBq/m^3, 2 orders of magnitude better than the best commercial radon detectors.

The detector construction consists of an electro-polished stainless steel chamber, with a volume of 70 litres, and a silicon PIN diode located at the top, as shown in Figure 6.1b. The detector electronics are housed in the lid of the detector separated from the detection chamber by a sheet of perspex with a feedthrough for the PIN diode. This design minimises the distance of the signal cable before pre-amplification as well as providing shielding from external noise. These electronics supply the bias voltage to the diode and provide the voltage rails for the multi-stage amplification of the signal and filter the HV power supply. Two gas flow valves, inlet and outlet, are located on either side of the detector. These have been coated with styrene butadiene

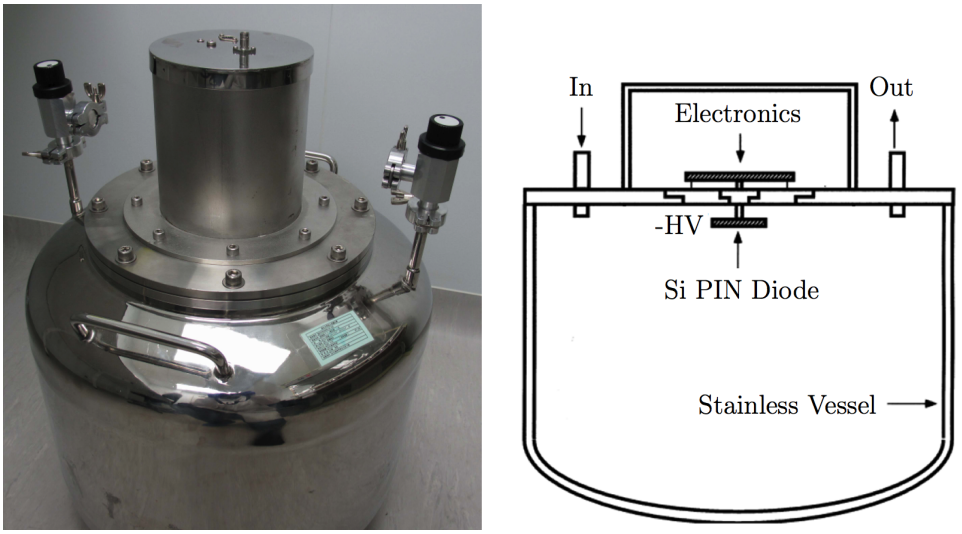

(a) Electrostatic radon detector in operation **(b)** Electrostatic radon detector schematic as shown in [53].

Figure 6.1: Electrostatic radon detector used for all measurements carried out on the radon emanation chamber.

rubber (SBR) to prevent radon diffusion. A negative high voltage is applied to the PIN diode (typically -1500 V) which generates an electric field inside the chamber.

The daughter nuclei of radon are predominantly positively charged ions. The fraction positively charged ions was measured to be 88% in 1913 [55] which is still in surprisingly good agreement with the recent measurement of 87.3 ± 1.6% [56]. These ions are attracted to the PIN diode by the applied electric field between the vessel and the diode. Once at the diode, some of the ions undergo α decays which are detected along with their energy. Decays of ^{218}Po, ^{214}Po and ^{210}Po are distinguishable by the amount of energy they deposit; 6.1MeV, 7.9 MeV and 5.4 MeV respectively. Another feature which separates ^{218}Po and ^{214}Po is the time is takes for their activity inside the detector to reach an equilibrium with the ^{222}Rn activity, as shown in Figure 6.2. The ^{218}Po reaches equilibrium with the ^{222}Rn quickly, however, ^{214}Po takes 4.5 hrs to reach equilibrium, this is due to it being further down the decay chain with two relatively long lived isotopes in between.

6.1.1 Detector Response

The signal from the detector electronics are passed to a NEMbox DAQ system (Wiener NEMbox SU706), which is a programmable field-programmable gate array (FPGA) designed to function as a NIM crate in a small, confined, bench-top unit.

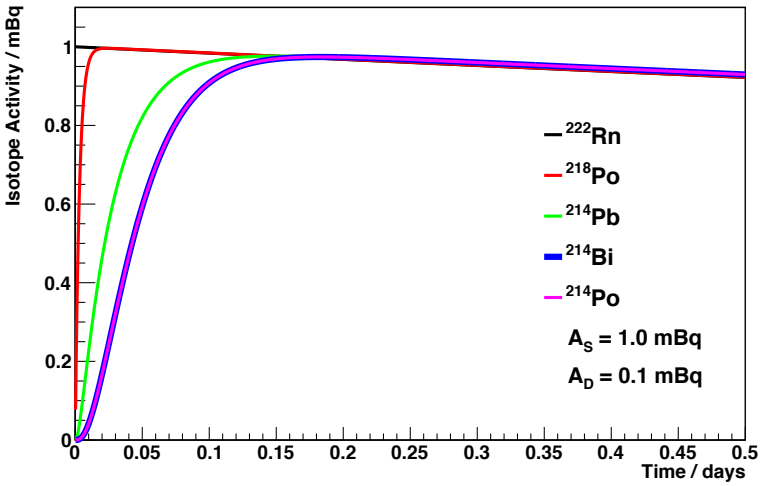

Figure 6.2: Activities of different isotopes in the ^{222}Rn decay chain with respect to time after introduction of 1 mBq of ^{222}Rn into a detector with 0.1 mBq background.

The NEMbox is used to trigger and digitise the pulse for storage as well as preventing re-triggering from after pulses. The signal pulses are recorded for offline analysis, which causes a dead time of ∼17 ms whilst the data is written to disk. The dead time was calibrated using a signal of known frequency and measuring the detector response, as shown in Figure 6.3. This dead time should have a negligible effect on all measurements except for some calibrations runs when the activity is high, when it must be taken into account.

6.1.2 Detector Efficiency

The detection efficiency of the electrostatic detector was calibrated using a source of known activity (1.32 kBq "flow-through" ^{226}Ra source by Pylon Electronics, RN-1025) and two separate methods. The first was to introduce a known amount of radon into the detector and measure the activity as it decays, the results are shown in Figure 6.4. Typically helium gas is chosen as the carrier gas over nitrogen, due to impurities such as nitrous oxide in the latter which can effect the detection efficiency by neutralising positive ions.

The detection efficiency can therefore be determined to be 31.6±1.6% and 27.1±1.4% for ^{214}Po and ^{218}Po respectively. This is in excellent agreement with the previous results, for example detection efficiency measured from over a year ago of 31.5±1.3% and 28.4±1.1% for ^{214}Po and ^{218}Po respectively. This suggests the detector has remained stable over the year even after the HV unit was changed. The associated

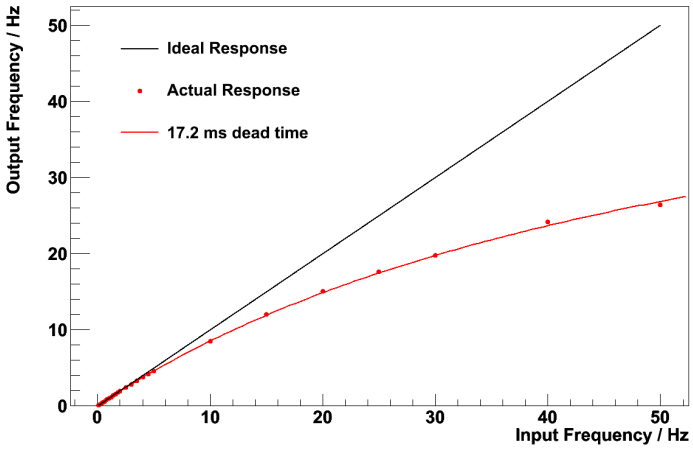

Figure 6.3: Response of DAQ system with varying frequencies. The red dots show the measured values.

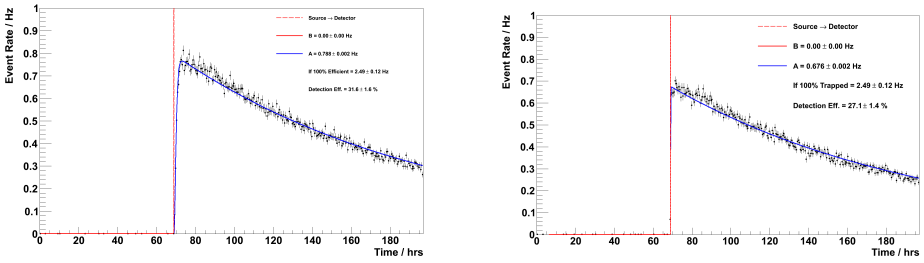

(a) ^{214}Po event rate. **(b)** ^{218}Po event rate.

Figure 6.4: The detected event rate of ^{214}Po and ^{218}Po when 2.5 Bq of radon is introduced into the detector volume.

errors are dominated by the uncertainties of the source activity. The maximum detection efficiency achievable is 50% for this type of detector, calculated from the solid angle, as this is the probability that the alpha from the decay will be emitted into the PIN diode, rather than away from it.

The ^{214}Po efficiency is higher than that of ^{218}Po as intermediate isotopes of ^{214}Pb and ^{214}Bi may also be collected onto the PIN diode, see Figure 6.5. The ^{214}Po is also less susceptible to neutralisation compared with ^{218}Po making the collection efficiency of ^{214}Po more stable in an environment where there are trace amounts of impurities. A typical background spectrum from the electrostatic detector is shown in Figure 6.6.

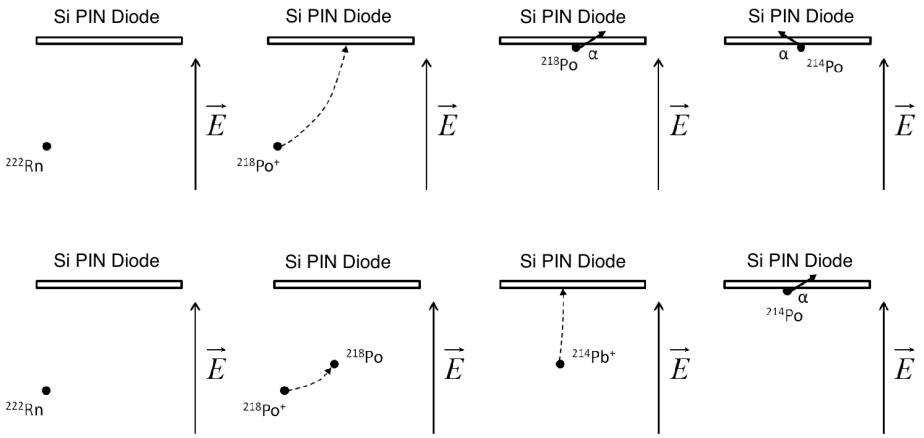

Figure 6.5: Ion collection and detection mechanism of electrostatic radon detectors.

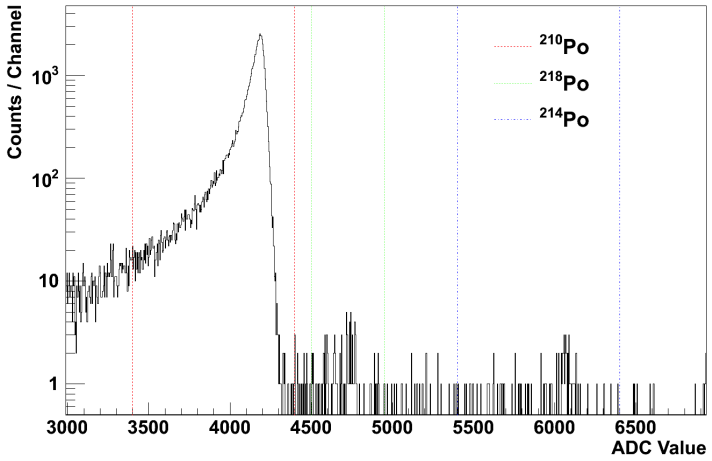

Figure 6.6: Background spectrum of the electrostatic detector with the ^{210}Po, ^{218}Po and ^{214}Po peak ranges displayed from left to right.

In addition, the ^{218}Po efficiency is also affected by the proximity of the ^{210}Po peak, which under normal low activity circumstances, is much larger. Even with the excellent resolution of the detector, there is still an overlap between the tail of the ^{218}Po and ^{210}Po, caused by α's which aren't fully contained in the active areas of the Si diode. Therefore, ^{214}Po is by far the best candidate for use in radon measurements.

With the helium replaced by nitrogen the detection efficiency is expected to be reduced as a result of extra impurities. This reduced efficiency was indeed observed with the detection efficiency measured to be 28.1 ± 1.1% and 22.3 ± 0.9% for ^{214}Po

and ^{218}Po respectively. The efficiency reduction is more severe for ^{218}Po as it is more sensitive to the increase in impurities.

As an extra precaution, a second calibration method was used to cross-check the efficiency results. This method required gas to flow continuously through the source and into the detector. The result of a flow through calibration is shown in Fig. 6.7. The calibration was conducted using nitrogen at a flow rate of 4.2 lpm. This translates to a detection efficiency of 29.4 ± 2.0 and 23.2 ± 1.6 for ^{214}Po and ^{218}Po respectively. This agrees closely with the efficiencies found using the "spike" method.

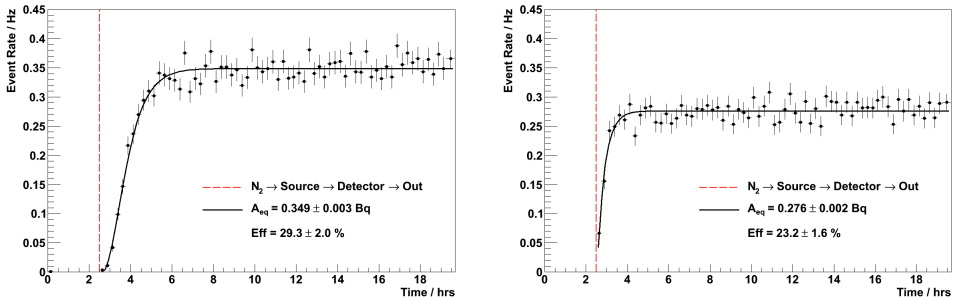

(a) ^{214}Po event rate. **(b)** ^{218}Po event rate.

Figure 6.7: Event rates of ^{214}Po and ^{218}Po for a flow through-type calibration run with a flow rate of 4.2 lpm of nitrogen. The black lines show the expected response taking into account the radon half life.

Although this method reduces the dependence on the uncertainties associated with the level of radon extracted from the source in the “spike" calibration, uncertainties in the flow rate and detector volume combine to make this calibration method less accurate overall.

Calibration Mode	Measurement Gas	Efficiency / % ^{214}Po	Efficiency / % ^{218}Po
Spike	He	31.5 ± 1.3	28.4 ± 1.1
Spike	N_2	28.1 ± 1.1	22.3 ± 0.9
Flow-through	N_2	29.3 ± 2.0	23.2 ± 1.6

Table 6.1: Electrostatic detector detection efficiency using helium and nitrogen as the carrier gas.

6.1.3 Detector Background Measurement

The ultimate sensitivity of the detector is not only limited by detection efficiency but is also heavily dependent on the background counting rate. Before each measurement, the background level inside the detector is measured to ensure the background is stable and can be correctly subtracted from any activity of radon observed.

Occasionally long background measurements are made to ensure the radon emanation levels inside the detector remain consistent. From a 25 day background measurement, the internal emanation of the detector, for ^{214}Po, was found to be 7.27 $\pm$ 0.53 counts-per-day (cpd). For this measurement, the detector was filled with helium, hence the intrinsic activity of the detector can be determined as 0.27 $\pm$ 0.02 mBq or 3.82 $\pm$ 0.28 mBq/m^3.

During background measurements the events are dominated by ^{210}Po which is similar in real measurements when the radon levels inside the detector are low. During calibration measurements when the radon level inside the detector is high, the situation changes and the events detected are dominated by ^{218}Po and ^{214}Po. Although the ^{210}Po rate does not provide any useful contribution to calculating the radon activity it does provide a reliable way of checking the stability of the detector and the DAQ system, the stays nearly constant over time with a half-life of 22.2 years [57]. The amount of intrinsic ^{210}Po does increase as more plates out onto the PIN diode over time. This build up could effect the sensitivity of ^{218}Po measurement as more ^{218}Po are drowned out by background noise.

6.1.4 Data Analysis Method

Each detected event is recorded via the NEMbox DAQ system as a text file for offline analysis. Each text file records the date and time of each of the 1000 events it contains with each event digitised into 1000 sample points. The text files are then analysed using ROOT.

The signal identification and analysis are separated into two steps. Firstly, a peak finding algorithm identifies the number of peaks present per event, along with their times and magnitude. From this, the events can be categorised into four distinct types as shown in Figure 6.8.

Signal events have only one peak (6.8a) and are passed straight to the second stage. BiPo events (6.8b), where ^{214}Bi and decay daughter ^{214}Po with a half-life of 164.3 μs, and pile-up events (6.8c) both have two peaks, they can be distinguished from each other by the magnitude of each of the two peaks. These events are rare, BiPo events contribute to only $\sim$1% of ^{214}Po events and pile-ups are only observed in calibration measurements. Finally, noise events have many peaks 6.8d which usually

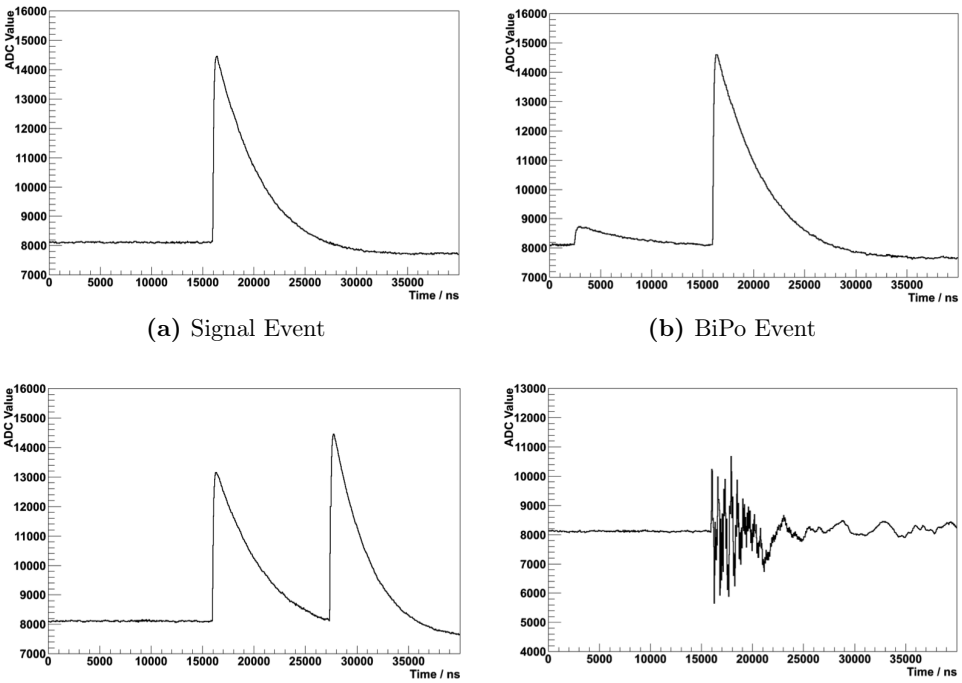

(a) Signal Event

(b) BiPo Event

(c) Pile-up Event

(d) Noise Event

Figure 6.8: The four types of events distinguished by the analysis algorithm.

have low amplitude and only occasionally have amplitude high enough to mimic a signal event.

To optimise extraction of signal amplitude each pulse is fitted with a function. The fitting function was defined as the expected form of a signal from the PIN diode after being passed through the pre-amplifier. This treatment removes any single peak event which does not have the normal signal event type.

The form of the true signal was found by shining a fast LED onto the PIN diode and reconstructing the output directly. The result was a signal that could be modelled as a sharp linear rise, followed by an exponential decay. The pulse shape parameters are fixed to measured values for this experimental setup, so that even single peaked events that do not originate from the PIN diode may be rejected.

An example of an event with a superimposed fit is shown in Figure 6.9, showing that the agreement between the actual and theoretical response is excellent.

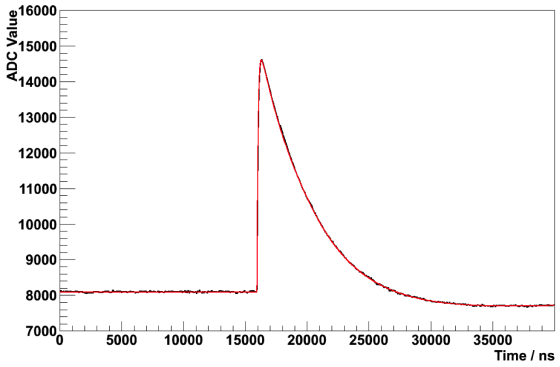

Figure 6.9: A signal event (black) with the fitting function superimposed (red).

6.2 Method for Determining Minimum Detectable Activity

To determine the sensitivity of the detector and the radon emanation chamber, a rigorous definition must first be defined for the sensitivity of a measurement. The definition used here is based on the method described by 'Radiation Detection and Measurement' by G. F. Knoll [58]. For a sample of unknown activity on a counting detector, the net counts, N_S can be calculated as:

$$N_S = N_T - N_B \tag{6.1}$$

where N_T is the total count with sample present and N_B is the background counts. To determine if the sample has any activity, compare N_S with the critical limit, L_C, which is defined as the activity level above which a positive measurement can be claimed with an associated confidence level. If $N_S > L_C$ then activity is present, if $N_S < L_C$ then no activity is present in the sample. In the case where both N_B and N_T are measured for sufficient time to result in Gaussian distributions, then the result of subtracting one from the other should result in a Gaussian which has a mean at the net number of counts with a standard deviation of:

$$\sigma_{N_S}^2 = \sigma_{N_T}^2 + \sigma_{N_B}^2 \tag{6.2}$$

In the case where no activity is present in the sample, then $N_B = N_T$ and the mean of N_S is zero with a standard deviation of:

$$\sigma_{N_S} = \sqrt{2}\sigma_{N_B} = \sqrt{2N_B} \tag{6.3}$$

Any measurement of signal will be false positive, therefore, L_C should be set sufficiently high to minimise the probability of N_S being greater than L_C to a predetermined level. For a false positive probability of less than 5%, L_C should be set at:

$$L_C = 1.64\sigma_{N_S} = \sqrt{2}\sigma_{N_B} = 2.326\sigma_{N_B} \tag{6.4}$$

In the case where activity is present in sample, the mean of N_S should be positive. So if no activity is observed, it would be a false negative result. The size of N_S required to minimise the probability of false negative result to a predetermined level is the detection limit, N_D. Again setting the probability of false negative to be less than 5%, this means 95% of the Gaussian distribution of N_D must be above L_C:

$$N_D = L_C + 1.64\sigma_{N_D} \tag{6.5}$$

where σ_{N_D} is the standard deviation of the Gaussian distribution about the N_D mean. Since $N_S = N_D$:

$$\sigma_{N_D}^2 = \sigma_{N_T}^2 + \sigma_{N_B}^2 = \left(\sqrt{N_T}\right)^2 + \left(\sqrt{N_B}\right)^2 = N_D + 2N_B \tag{6.6}$$

$$\sigma_{N_D} = \sqrt{N_D + 2N_B} \tag{6.7}$$

Combining (6.7) and (6.4) into (6.5) gives:

$$N_D = 1.64\left(\sqrt{2N_B} + \sqrt{N_D + 2N_B}\right) \tag{6.8}$$

Solving for N_D gives:

$$N_D = 2.71 + 4.65\sqrt{N_B} \tag{6.9}$$

The detection limit is determined prior to measurement as the minimum counts required from the sample to ensure a false negative probability of less than 5%.

6.2.1 The MDA for an Electrostatic Detector

To obtain an MDA for the electrostatic detector at the Mullard Space Science Laboratory (MSSL) the expected number of signal and background events for a measurement must be found. The detector background, A_D, is intrinsic. The number of radon atoms in the detector at a given time can be found by solving the differential equation:

$$\frac{dN}{dt} = -\lambda N + A_D \tag{6.10}$$

It can be seen that:

$$\frac{d}{dt}(e^{\lambda t}N) = e^{\lambda t}(\frac{dN}{dt} + \lambda N) = e^{\lambda t}A_D \tag{6.11}$$

Therefore:

$$e^{\lambda t}N = \int e^{\lambda t}A_D dt = \frac{A_D}{\lambda}e^{\lambda t} + C \tag{6.12}$$

Assuming the detector has been flushed before measurement, N = A_S/λ at t=0, where A_S is the radon activity. Therefore C = A_S/λ - A_D/λ and

$$N = \frac{A_D}{\lambda}(1 - e^{-\lambda t}) + \frac{A_S}{\lambda}e^{-\lambda t} \tag{6.13}$$

which is the sum of the background term and the exponentially decaying signal term.

It is a reasonable approximation to consider the signal events to come purely from ^{222}Rn decay without considering the decay chain to ^{214}Po. This approximation can

be made as the intermediate isotopes of the decay chain have relatively short half lives compared to any real measurement time. For the number of signal events, S, expected to have been detected after a given time, T, in a detector with detection efficiency, ϵ, set the detector background to zero and

$$S = \epsilon \int_0^T \lambda N dt = \epsilon \int_0^T A_S e^{-\lambda t} dt = \epsilon \frac{A_S}{\lambda}(1 - e^{-\lambda T}) \tag{6.14}$$

Similarly for the number of expected background events, B, the signal activity is set to zero so that

$$B = \epsilon \int_0^T \lambda N dt = \epsilon \int_0^T A_D(1 - e^{-\lambda t}) dt = \epsilon A_D T - \frac{\epsilon A_D}{\lambda}(1 - e^{-\lambda T}) \tag{6.15}$$

The efficiency of the detector has been measured as ϵ ~31.5% and the background measured to be ~7.3 cpd, equivalent to $A_D = 0.27$ mBq. From this the MDA for the detector can be calculated by first finding B using equation (6.15), then S_0 using equation (**??**) for a given confidence level. Finally equation (6.14) was used to convert S_0 into the MDA. The detector MDA vs measurement time, T, is shown in Fig 6.10.

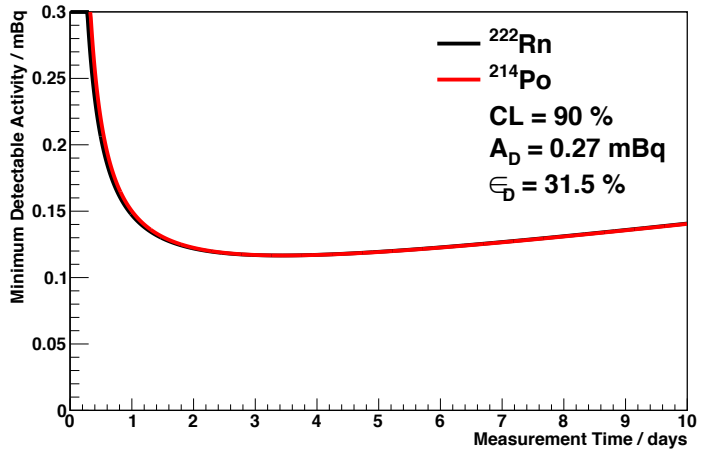

Figure 6.10: The MDA for the electrostatic detector vs the duration of the measurement. The ^{222}Rn (black) and ^{214}Po (red) results are shown.

As it can be seen, the sensitivity is very low at short measurement times since there has been no time for any radon to decay. As the measurement time increases, the MDA falls rapidly until a shallow minimum is reached after ~3 days. After this the

increasing number of background counts takes effect and the MDA increases again. From this plot, the MDA for the detector can be extracted to be 0.12 mBq or 1.7 mBq/m^3.

Since detectors are often subject to contamination, the background levels can vary significantly between detectors. Therefore the relationship between the MDA and the background level can be studied, as shown in Fig 6.11a. From this, it can be seen that after an initial rapid rise the MDA increases almost linearly with background levels. The MDA was calculated by finding the optimal measuring time as shown in Fig 6.11b. As expected, the measurement time decreases rapidly as background levels increase in order to minimise the effect of the background on the measurement.

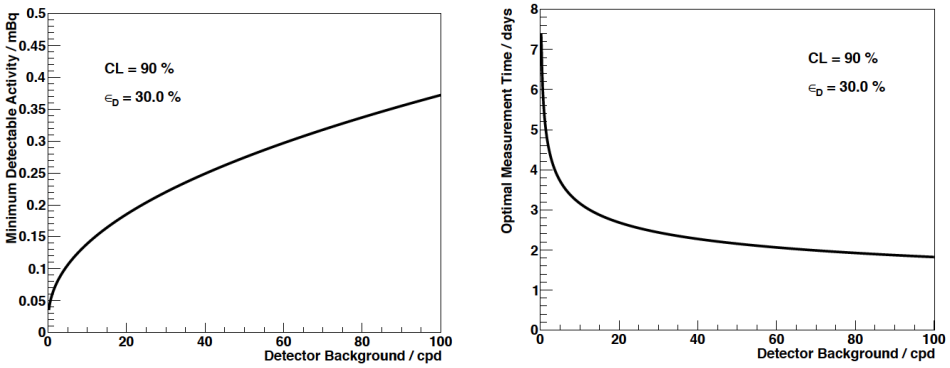

(a) Background vs MDA. **(b)** Optimal measurement time vs MDA

Figure 6.11: Plot(a) shows the MDA for the electrostatic detector at 90% CL with an efficiency of 30 % for various background levels. Plot(b) shows the optimal measurement time to find the minimum value of the MDA for the particular background level.

6.3 The Radon Emanation Chambers

A radon emanation chamber was constructed, using stainless steel, in Alabama, United States. It was then assembled and tested at UCL in order to measure the level of radon emanation. The emanation chamber, shown in Fig 3.1, is 152.4 mm in length and 146 mm in diameter resulting in an internal volume of approximately 2.6 litres.

The emanation chamber has two stainless steel flanges, one on each side of a stainless steel tubular body, sealed using copper gaskets. The chamber was vacuum tested to ensure it was airtight, this is done in two ways. Firstly, once a sample is sealed inside the chamber helium was used to flush the emanation volume to remove any

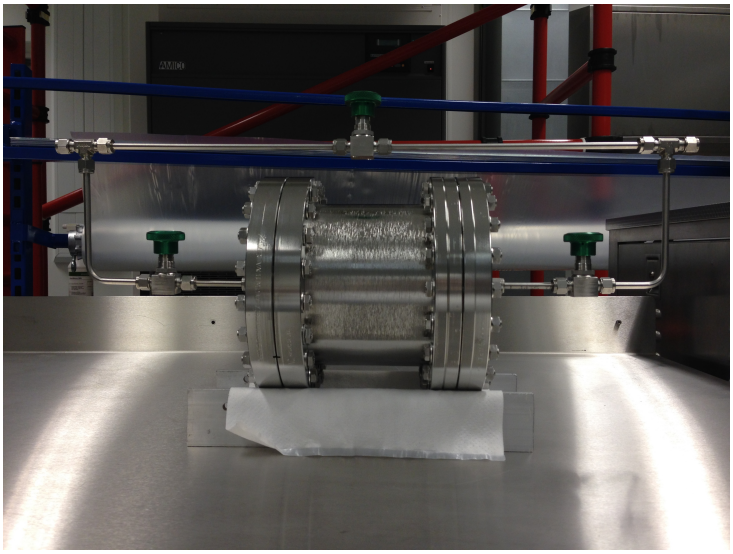

Figure 6.12: The radon emanation chamber fully assembled at MSSL.

residual air. A helium leak detector (GasCheck Tesla Helium Leak Detector, ion science) was then used to test all the connections to ensure no leaks above 10^{-6} cc/s were observable. Then the chamber was then sealed under 0.5 bar of pressure and the same leak tests were repeated again to ensure no leaks above 10^{-6} cc/s were observable.

For each new sample the emanation chamber is purged using helium for 200 times the volumes of the chamber (VC) to ensure other gases are completely removed, before it is sealed under atmospheric pressure. The chamber is then left to emanate for at least 1 week before the gas inside is transferred directly into the electrostatic detector for measurement. For details on the procedure for emanation measurement, see document titled 'LUX Emanation Chamber Measurement Results'.

6.3.1 Initial Leak Tests

Once the chamber was cleaned, using isopropanol (IPA) and assembled (Fig 6.13) a series of tests were conducted to determine if any leaks were present. Firstly, the chamber was placed under 100 mbar of pressure and left for 24 hours, after which no drop in pressure was detected. This pressure was then increased to 1 bar and left overnight, still no drop in pressure was observed.

With the chamber under 1 bar of pressure a helium detector was used to measure the level of helium detectable around the joints of the emanation chamber. This showed the chamber to well sealed with no leaks detected above 10^{6} cc/s.

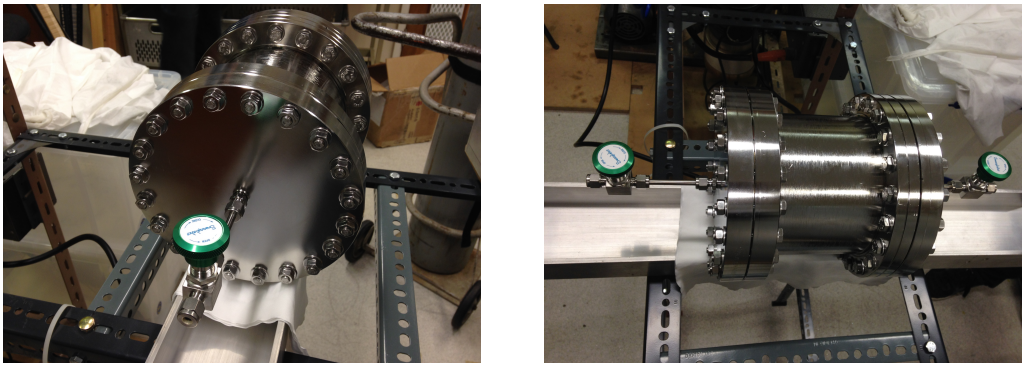

(a) Chamber front view. **(b)** Chamber side view.

Figure 6.13: The radon emanation chamber being assembled with Swagelok fitting attached.

6.3.2 Background Measurement

Having established that the radon emanation chamber was leak free the chamber was then transported to MSSL where it was reassembled. It was then connected to the radon detector directly, schematic shown in Figure 6.14. The entire line with the chamber attached was flushed, see Figure 6.14a, using helium and a leak test was again performed to ensure the line was air tight. The chamber itself remained sealed for the entire process. After flushing with helium for 100 times the VC the chamber was sealed under atmospheric pressure in order to measure the background emanation from the chamber itself.

After 30 days when the level of radon inside the chamber had reached equilibrium, it was flushed into the detector using 25 litres of helium, $\sim$ 6.25 volumes of the chamber. The process is shown in Fig 6.14. This sample was measured over a week and the results are shown in Fig 6.15.

From the results shown in Fig 6.15, a limit may be placed on the emanation chamber background, calculated using:

$$A_L = \frac{1.64 \times R_D}{86400} \tag{6.16}$$

where A_L is the limit at 90% confidence level and R_D is the detected rate. Correcting for the detection efficiency of the detector and the transfer efficiency for the true activity A_T;

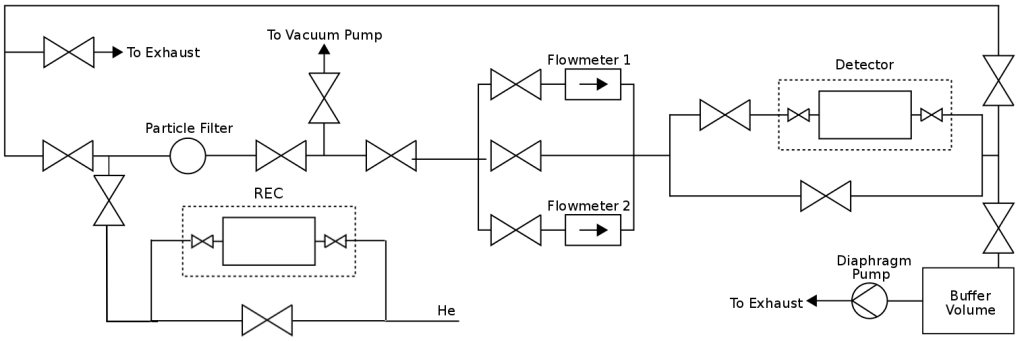

(a) Schematic diagram of the design of the entire RnCL built for SuperNEMO measurements.

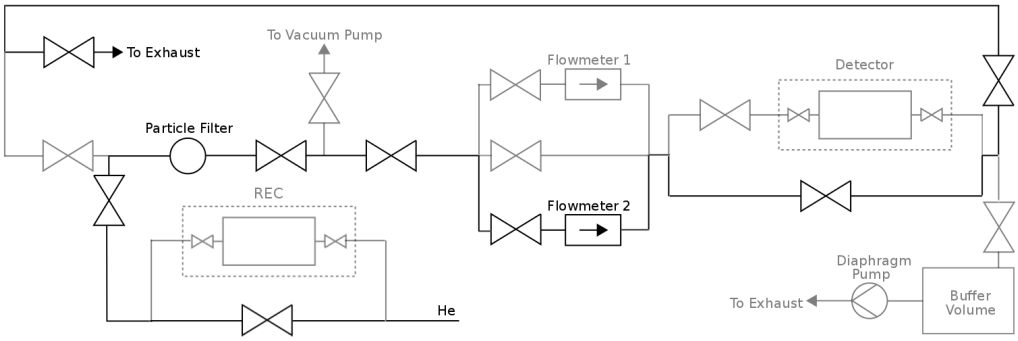

(b) The sections of the RnCL used when during the flushing process.

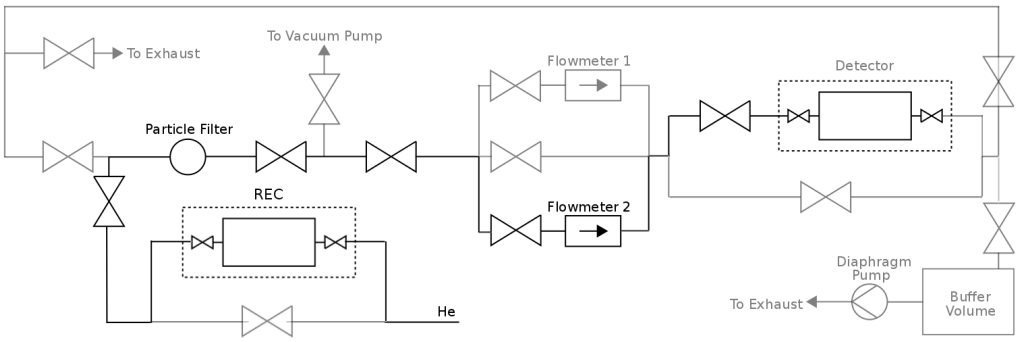

(c) The sections of the RnCL used when transfering the gas from inside the emanation chamber into the detector.

Figure 6.14: Schematic diagrams showing the RnCL and the sections used during the flushing and transferring processes.

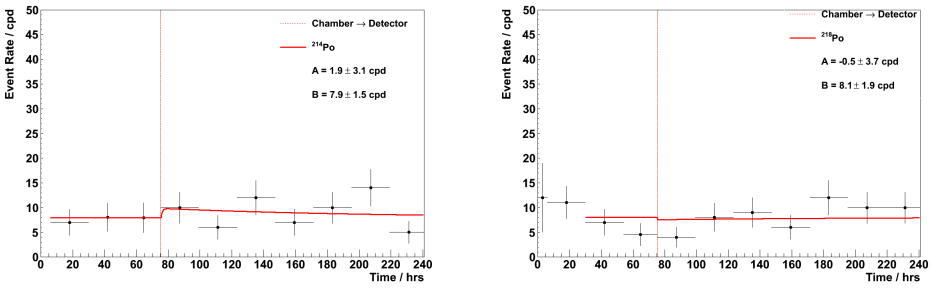

(a) ^{214}Po event rate. **(b)** ^{218}Po event rate.

Figure 6.15: The detected event rate of ^{214}Po and ^{218}Po as measured by the alpha detector.

$$A_T = \frac{A_L}{\varepsilon(1 - e^{-N_v})} \tag{6.17}$$

Where N_v is the number of volumes of the chamber flushed into the detector. Finally, correcting for the initial activity levels from equilibrium;

$$A = A_T(1 - e^{-\lambda t}) \tag{6.18}$$

Hence, the sensitivity limits on ^{214}Po and ^{218}Po are;

$$^{214}\text{Po} = 0.187 \text{ mBq} \tag{6.19}$$
$$^{218}\text{Po} = 0.246 \text{ mBq} \tag{6.20}$$

6.3.3 The Radon Harbouring Hypothesis

During measurements of materials which are highly diffusive to radon, it was observed some residual radon from the atmosphere can be diffused into the materials such as the duracon and scintillator. Even after flushing such materials can still out gas radon hence producing a higher activity value.

This is known as the radon harbouring hypothesis and it was demonstrated using the radon emanation chamber and a sample of duracon. The sample was placed

into an emanation chamber which was then purged with 200 volumes of radon free helium and left to emanate at atmospheric pressure. After 7 days, the gas inside the chamber was transferred into the radon detector for measurement producing a positive result, as shown in Figure 7.6. After transfer the chamber was again flushed with helium and sealed at atmospheric pressure. After 10 more days (17 days inside chamber) a second transfer was made of the gas inside the chamber to the radon detector which showed no positive signal, as shown in Figure 7.6. This result is of

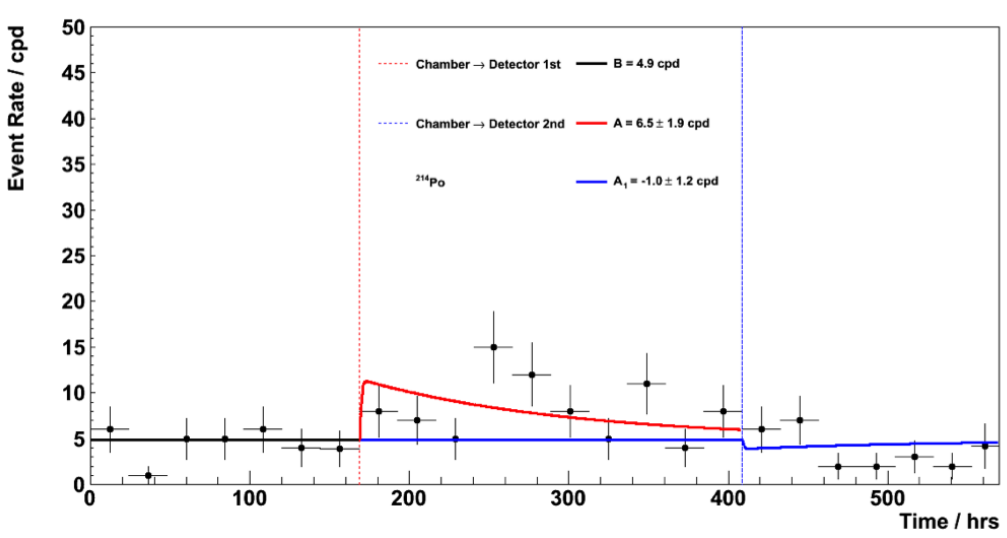

Figure 6.16: The measured Po214 activity from first and second transfer, demonstrating the radon harbouring hypothesis. The result from the first transfer is fitted with a red line whilst the result from the second transfer is fitted with a blue line.

particular interest as there are components inside the tracker that are made from materials which are opaque to radon.

6.4 The Radon Concentration Line

The modified electrostatic radon detector has demonstrated a stable low background making it one of the most sensitive compact detectors in the world. However, it is still one order of magnitude away from the SuperNEMO radon requirements. Therefore, a new technique and system had to be developed in order to further improve its sensitivity.

A radon trapping system known as the Radon Concentration Line (RnCL) was developed to be used in conjunction with the electrostatic radon detector. The

RnCL system essentially consists of a stainless steel trap containing ultra radio-pure activated carbon which is cooled to -50 °C. The cooling significantly improves the charcoal's ability to capture radon. Large volumes of gas can be flowed through the trap where the radon is adsorbed. After the gas volume to be measured has passed through the charcoal trap, it is sealed and the concentrated radon sample can then be heated, releasing the radon, which can then be flushed into the electrostatic detector for measurement.

The radon concentration line was built to increase the sample volume of gas measurable using the radon detector. This significantly increased the sensitivity of the detector in terms of Bq/m^3. The design of the RnCL is similar to the MoReX line [59] developed in Heidelberg, however, the design has been simplified for increased portability. The setup of the RnCL is shown in Figure 6.26

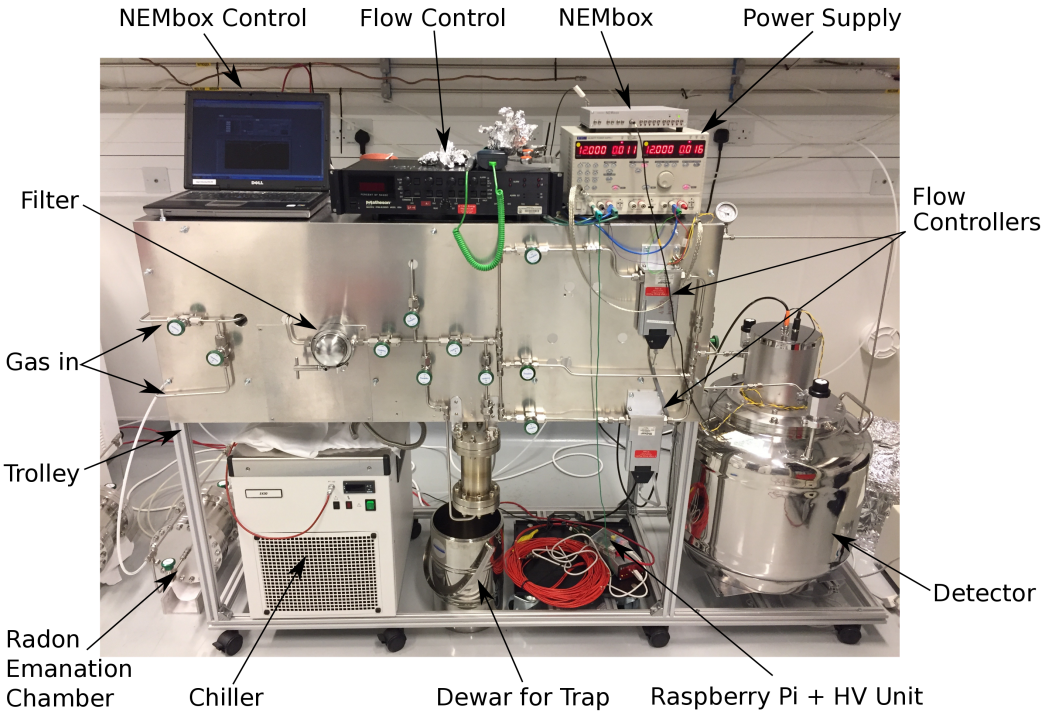

Figure 6.17: The radon concentration line setup.

The RnCL was designed with vacuum capability and a vacuum pump attachment. However, the detector demonstrated better and more stable performance when the purge gas is simply transferred directly with the detector at atmospheric pressure. Due to the small volume of the trap 25 litres of helium is enough to ensure more than 100 volume replacements and almost complete transfer of the released radon into the detector. The increase in operational pressure from 1 bar to 1.36 bars was shown to have negligible effects on the detector performance.

An additional buffer volume and a diaphragm pump was added to the RnCL exhaust which enabled the possibility to actively draw gas through the line. This was necessary for measurement of gas volumes at low or atmospheric pressures as at least 0.2 bars of overpressure is required to achieve the nominal flow rate, 10 lpm, through the RnCL. Therefore, the pump is essential as the completed trackers cannot safely accommodate a large over-pressure.

6.4.1 Modifications to the RnCL

The initial rendition of the RnCL successfully demonstrated the ability to surpass the sensitivity required for radon measurements of the SuperNEMO tracker. However, there were draw backs such as several sources of uncertainty associated with measurement results and longer time per measurement. In order to further improve the trapping and transfer efficiency of radon in large gas volumes as well as minimising systematic uncertainties several modifications were made to the RnCL which was re-calibrated to quantify the effects.

6.4.2 Gas Line Filter

A series of particle filters were used to prevent any particulates contaminating the electrostatic detector. However, high background levels of radon emanation were observed which were attributed to a gas line filter made of a black plastic material. An emanation test was therefore performed to test this hypothesis, the result showed the activity of the gas line and particle filter to be 7.4±1.0 mBq.

The gas line filter was replaced with a Swagelok stainless steel filter with 0.5 micron pore size. The entire gas line was filled with helium and sealed at atmospheric pressure for radon to build up from emanation. Then, after 5 days, the gas was transferred directly into the detector for measurement. The results are shown in Figure 6.18.

From this, an activity of 1.8±0.3 mBq can be extracted which suggests the particle filter was indeed the major contributor to the radon background.

6.4.3 Trap Cooler

A new cooler (EK90 Immersion Cooler by Thermo Scientific) was purchased which was capable of reaching temperatures of -90 °C instead of -30 °C previously. This lower temperature should increase the trapping efficiency of the activated carbon, this is shown in Section 6.4.6.

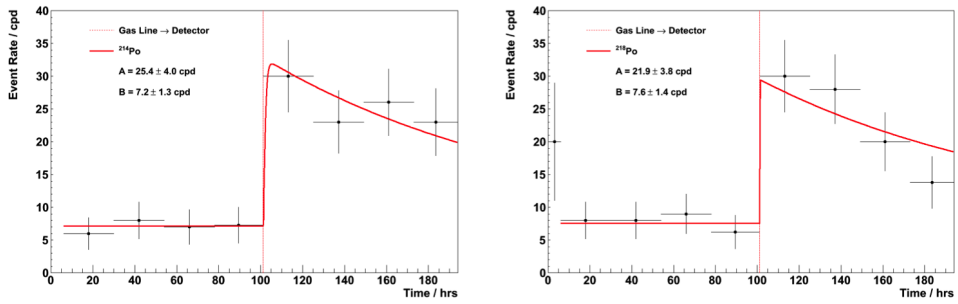

(a) ^{214}Po event rate. **(b)** ^{218}Po event rate.

Figure 6.18: The detected event rate of ^{214}Po and ^{218}Po before and after gas from the gas line was transferred (vertical red line) into the detector for measurement.

6.4.4 Trap Modification

The carbon trap underwent a complete redesigne to improve the trapping and transfer efficiency. Due to the design of the old carbon trap it was very difficult to ensure all the Swagelok connections were tightly sealed and it was impossible to carry out a leak test on the system. During operation the pressure required to flow gas through the trap at a constant rate went up over a period of 12 months of use. This also coincided with a fall in the trapping efficiency which led to the hypothesis that a blockage could have occurred at the gas outlet and a leak could be present at a point above the active carbon as shown in Figure 6.19.

A new trap was developed in order to minimise the risk of a leak developing in the pipe work within the trap. It has a detachable base flange which allows easy access to tighten the pipe work, as shown in Figure 6.20.

The new trap has a slightly larger volume, 0.5 l compared to 0.4 l of the old trap. From the transfer some activated carbon was also lost, resulting in 52.5 g of carbon in the new trap instead of the 57 g present in the old trap. The new trap was installed onto the RnCL and the trap emanation background was measured.

To determine the trap background the trap was first cleared by heating to above 200 °C and flushing continuously with helium. Then the trap was sealed with helium inside under atmospheric pressure to emanate for 7 days. After 7 days, the gas inside the trap is transferred into the detector using helium for measurement. The resultant plots are shown in Figure 6.21.

The activity was calculated to be 0.48±0.14 mBq and 0.42±0.14 mBq for ^{214}Po and ^{218}Po respectively. This is slightly higher than the old trap which was found to be 0.23±0.11 mBq, but the two results are consistent within ∼1.3 sigma.

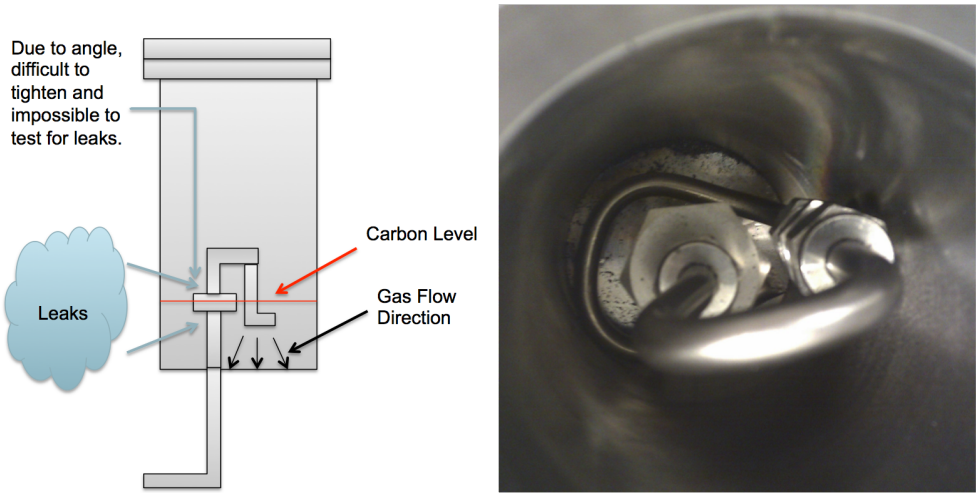

(a) Possible issues with the old carbon trap. **(b)** Inside of the old trap.

Figure 6.19: The schematic on the left shows the possible issue with the old trap design which can be compared to the real picture taken of the inside of the carbon trap.

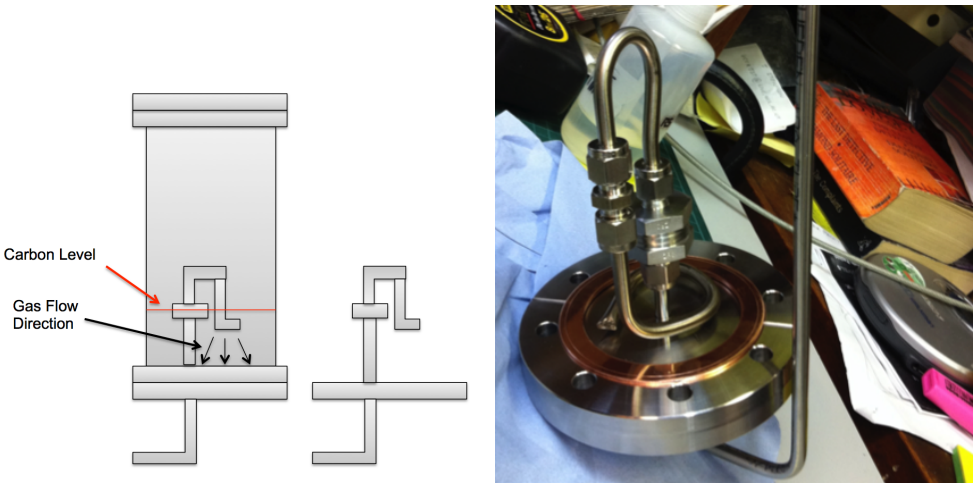

(a) New trap schematic. **(b)** Base flange with pipework.

Figure 6.20: The new carbon trap design which has a detachable base flange thus allowing easy access for pipe work installation.

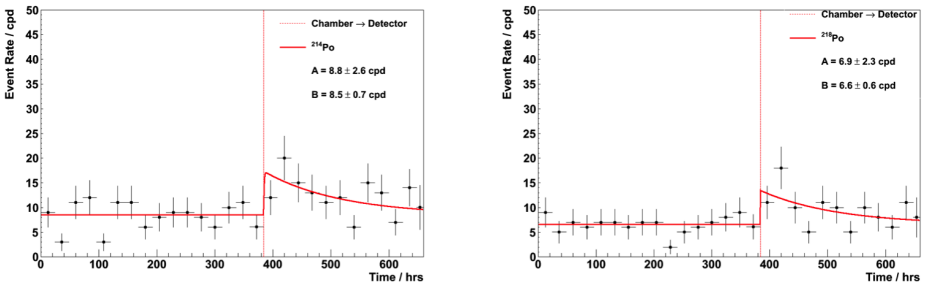

(a) Event rate of ^{214}Po. **(b)** Event rate of ^{218}Po.

Figure 6.21: The new carbon trap backgrounds.

6.4.5 HV Upgrade

The RnCL was previously run on a multi channel CAEN HV unit and it required a very stable supply of 1500 volts. Large shifts were observed in the output spectrum from the electrostatic detector which was traced back to an unprecedented level fluctuations on the output of the Caen HV unit. A single channel HV unit was purchased as the replacement which was connected and controlled using a Raspberry Pi computer. This enables remote monitoring of HV voltages and in case of large voltage fluctuations, an email alert can be sent out. The new HV unit also provides the added bonus of making the RnCL as completely stand alone unit.

6.4.6 RnCL Calibrations

To quantify the effects of all the modifications a flow-through calibration using nitrogen was carried out with the new HV unit, cooler and radon trap. The idea of the flow-through calibration is to mimic the same conditions as a real measurement of the SuperNEMO tracker using the RnCL. The steps are as follows and the schematic can be seen in Figure 6.22;

1. First attach the radon source (used previously for the spike calibration) into the RnCL setup, as shown in Figure 6.22a, then flush with nitrogen at 7 lpm continuously to exhaust in order to remove the built up radon.

2. Flush the source for 3 hours, to ensure all residual radon is removed, then flow nitrogen through the radon source and the detector, then out to exhaust at a constant rate of 7 lpm, as shown in Figure 6.22b. Measure the output activity for ∼24 hours to ensure the activity through the detector remains stable. This follow rate was

selected as it is the maximal flow rate which can be achieved during SuperNEMO tracker measurements.

3. After 24 hours, divert the gas from the source through the trap first before the detector and then out to exhaust, maintaining the same flowrate of 7 lpm, as shown in Figure 6.22c.

4. After 20 hours of trapping seal the trap and source.

5. Start to heat the trap for the transfer, in the meantime remove the radon source and clear the detector by flushing continuously with helium for 10 volume replacements to remove any residual radon, as shown in Figure 6.23a. Once cleared, seal the detector under atmospheric pressure.

6. Once the trap has reached above 200 °C, transfer the gas contents into the detector for measurement, as shown in Figure 6.23b.

From this calibration all the necessary information for a tracker measurement can be extracted. The activity in the radon detector during the flow through calibration run can be seen in Figure 6.24. The activity in the detector from steps 1 to 5 can be seen in Figure 6.24a and Figure 6.24c is the same but extended to include step 6.

The result from this calibration can be compared to the same calibration measurements taken before the modifications were made to the RnCL, see Figure 6.24b and Figure 6.24d. Comparing Figure 6.24a and Figure 6.24b, in each case the radon activity reaches a stable level in the first 20 hours. Then when the trap is introduced into the system the level drops sharply in both cases, slightly lower in the modified system suggesting better trapping efficiency. The key change seen after the modifications is in the rate of activity rises after the initial fall. In the case of the old trap there is almost an equally sharp rise which slightly tales off, whereas in the modified trap the rise is more gradual. The hypothesis for this loss of trapping efficiency is due to the activated charcoal becoming saturated with radon. The radon is released and then captured, in this way it is pushed along the charcoal until it is finally free to recombine with the carrier gas post trap. By lowering the trap temperature the charcoal can hold more radon hence takes longer to become saturated.

To quantify the trapping efficiency, the specific activity at the output of the source must first be calculated;

$$a_S^{eq} = \frac{A_S}{f_S/\lambda} = \frac{1.32 \pm 0.05\text{kBq}}{55.7 \pm 2.7\text{m}^3} = 23.7 \pm 1.5\text{Bq/m}^3 \tag{6.21}$$

Where A_S is the activity of the source and f_S is the flowrate through the source, in this case 7 lpm. The equilibrium activity inside the detector can be determined using

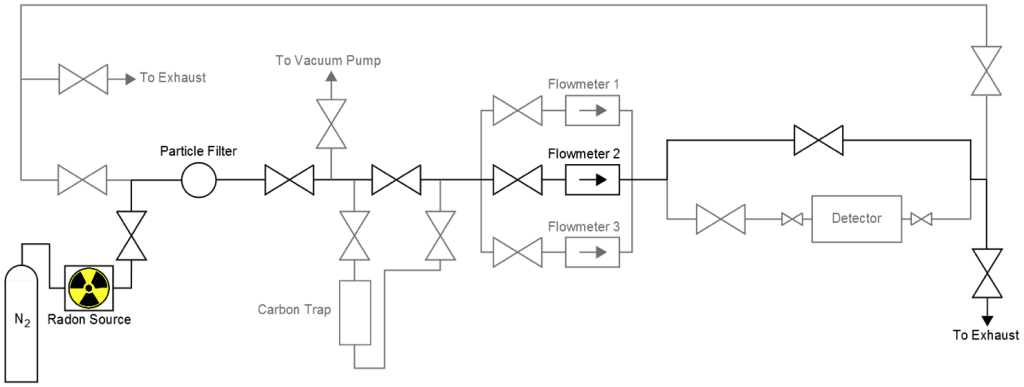

(a) Flushing the radon source to remove any residual radon build up.

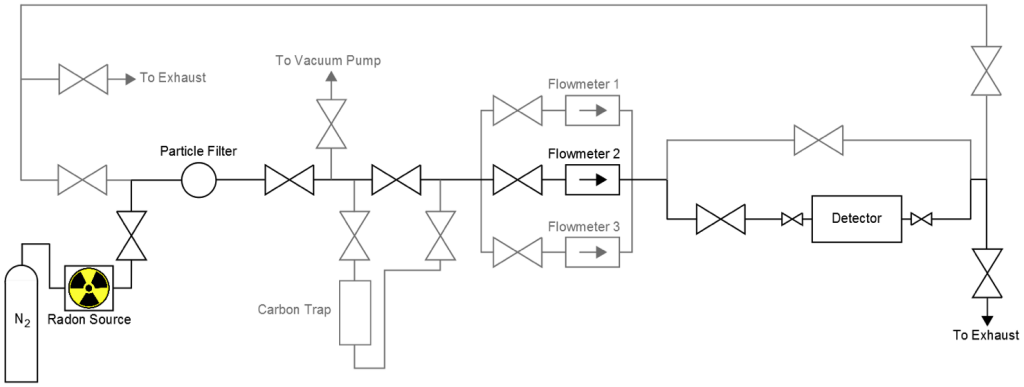

(b) Nitrogen carrying a know activity of radon was flowed through the detector.

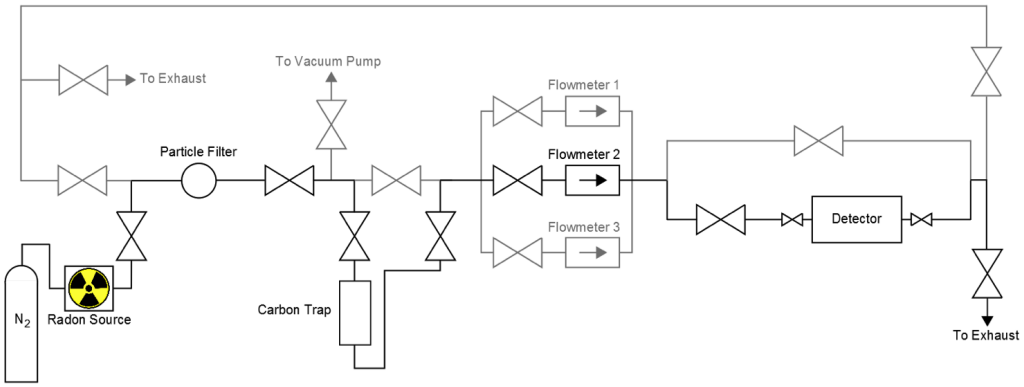

(c) The sections of the RnCL used for trapping of radon from the carrier gas.

Figure 6.22: Schematic diagrams showing the RnCL setup during a flow through calibration using a radon source.

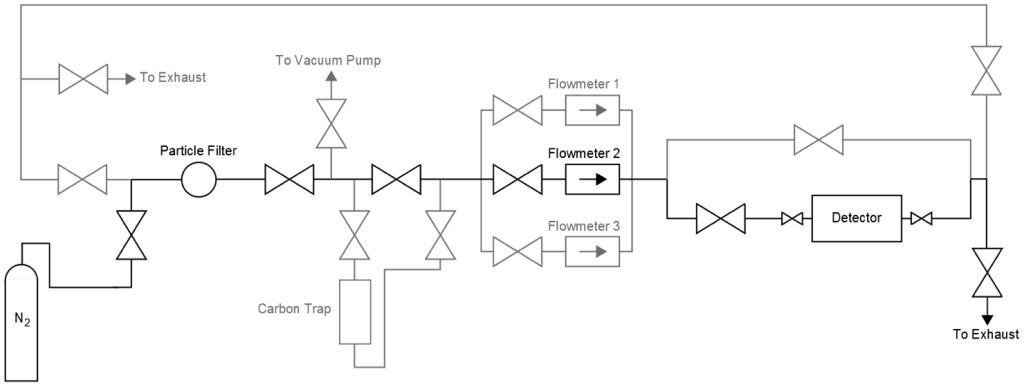

(a) Clear the electrostatic detector by flushing with nitrogen.

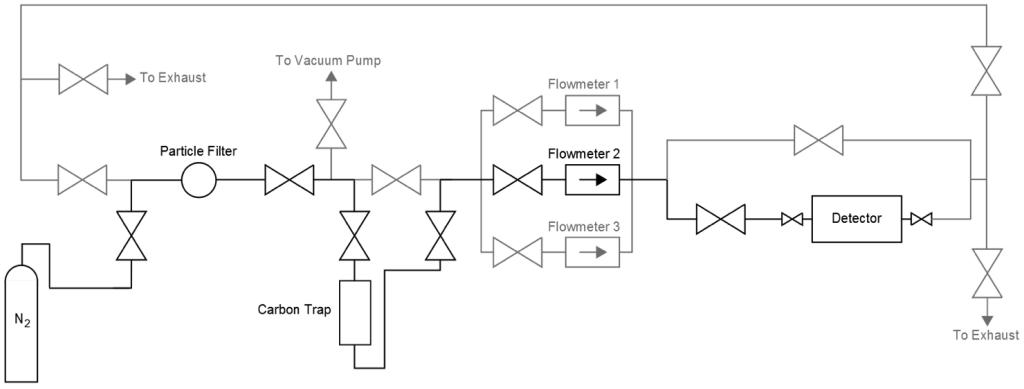

(b) Transfer adsorbed radon from charcoal trap to detector for measurement via gas purge.

Figure 6.23: Schematic diagrams showing the RnCL setup during gas transfer stage of flow through measurement after trapping.

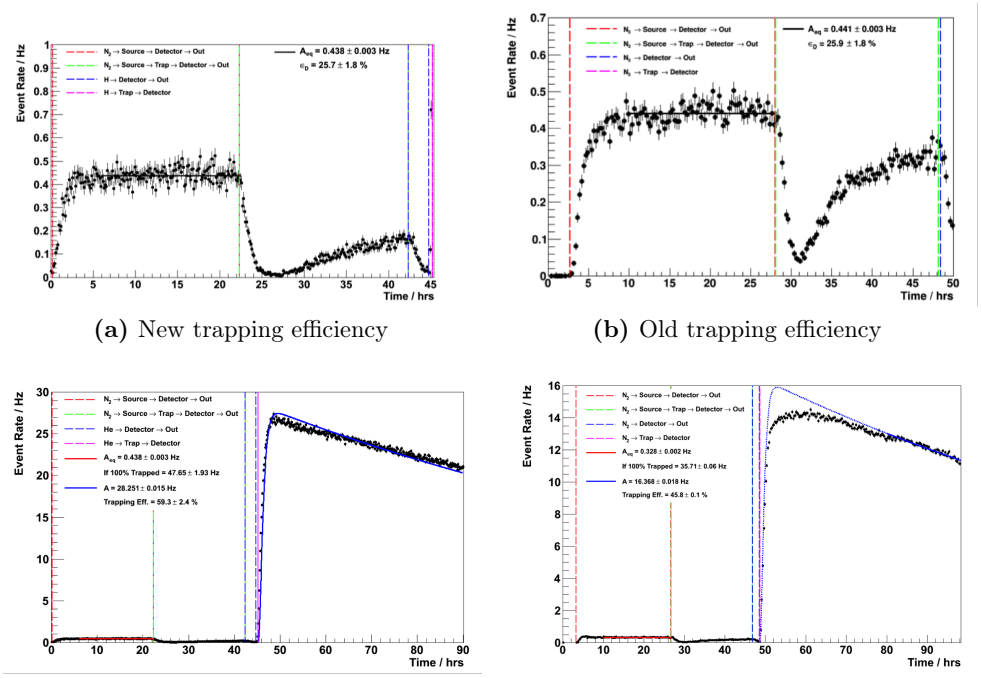

(a) New trapping efficiency

(b) Old trapping efficiency

(c) New trapping/transfer efficiency

(d) Old trapping/transfer efficiency

Figure 6.24: Comparison of the activity inside the radon detector using the new (plots a and c) and old (plots b and d) carbon trap.

$$A_D^{eq} = \frac{A_S}{1 + f_S/\lambda V_D} = 1.7 \pm 0.1\text{Bq} \tag{6.22}$$

The measured event rate inside the detector at equilibrium was 0.438 Hz which translates to a detector efficiency of 27.5 ± 1.8%. This is consistent with the efficiency found during flow through calibration of 29.3 ± 2.0%.

By monitoring the activity of the gas after it has gone through the carbon trap it is possible to then calculate the amount of radon trapped within the carbon. Taking the ratio between this value and an idealised case where 100% of the radon is trapped gives the trapping efficiency as a function of time which is shown in Figure 6.25.

From Figure 6.25 it can be seen that the initial trapping efficiency is very close to 100% but falls off with time. This could be as a result of the radon retention time of the carbon material. The amount of radon after 20 hours can then be compared with what is observed inside the detector after the transfer to obtain the transfer efficiency.

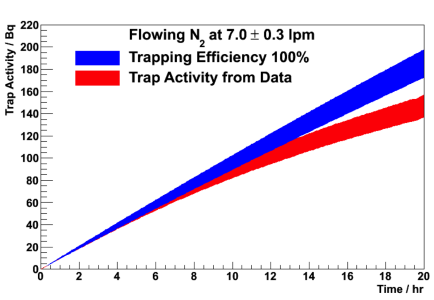

(a) Radon activity in new trap.

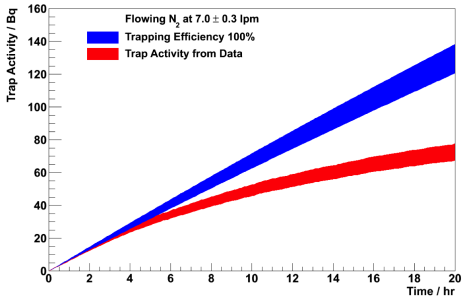

(b) Radon activity in old trap.

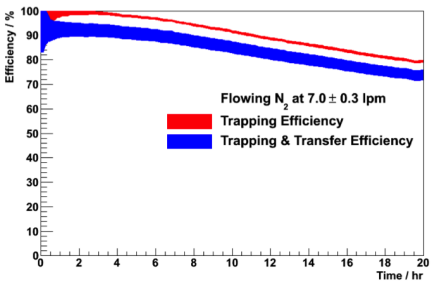

(c) Trapping and transfer efficiency.

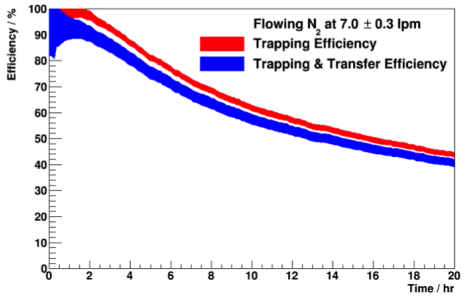

(d) Trapping and transfer efficiency.

Figure 6.25: Comparison of trapping and trapping/transfer efficiencies of the new (plots a and c) and old (plots b and d) carbon trap.

It can be seen from Figure 6.25c and Figure 6.25d that the modifications to the trap have resulted in almost a factor 2 improvement in the trapping and transfer efficiency of the RnCL system.

6.5 Radon Concentration Line Sensitivity

The MDA of the electrostatic detector was defined in Section 6.2.1. The RnCL is able to improve upon this MDA in terms of Bq/M^3 by allowing the measurement of radon from a larger gas volume inside the same electrostatic detector. Therefore, MDA improves as a function of volume of gas as shown in Figure 6.25c.

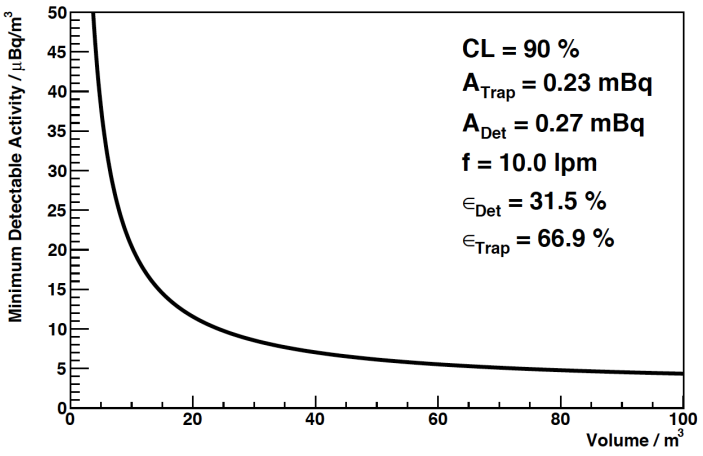

Figure 6.26: The MDA as a function of gas volume.

A significant improvement can be seen and sensitivities as low as 5 $\mu Bq/m^3$ can be achieved. There is however diminishing returns as volume of gas required to improve MDA increases exponentially. At the calibrated volume of 8.4 m^3 a sensitivity of $<$ 40 $\mu Bq/m^3$ can be reached which is more than enough to meet the SuperNEMO demands.

Chapter 7

Radon Measurements For SuperNEMO

"I'm intimidated by the fear of being average."
- Taylor Swift

The radon detector and the RnCL have both demonstrated excellent performance and, when used in conjunction, the capability to reach the target radon sensitivity required for the SuperNEMO demonstrator. This allows the monitoring of radon emanation from quarter trackers during construction providing essential information for radon budget.

The key measurements carried out using the radon detector alone, and in combination with the RnCL, are detailed here, including measurement of three out of four demonstrator quarter trackers, radon emanation from the SuperNEMO gas system and radon content of SuperNEMO gases.

7.1 Gas Cylinders

A measurement programme of gas cylinders was undertaken to quantify their radon content, under the same conditions as during a tracker measurement. This was essential in order to disentangle the radon activity of the carrier gas from radon emanated in tracker measurements. It was shown that the gas used in tracker measurements is one of the main contributors to the radon background.

7.1.1 Cylinder Activity

The information of interest from gas cylinders is the specific activity in Bq/m^3. As the physical volume of a cylinder remains constant but the volume of gas contained

within it changes as it's emptied, if the radon is evenly distributed, the specific activity of the output gas can be modelled as;

$$\frac{dN_G}{dt} = A_G - \lambda N_G - \frac{fN_G}{(V_G - ft)} \tag{7.1}$$

where N_G is the number of radon atoms in gas cylinder, A_G is the specific activity of the gas and V_G is the total volume of gas (at STP) contained in the cylinder at the start of the measurement. Depending on the flow rate a fraction of radon is removed from the bottle which is replaced with emanated radon. To ensure the radon measured is from emanation of the cylinder alone and not as a result of radon introduced during the filling, each cylinder was left sealed for more than 3 weeks before being measured to ensure the radon activity is at equilibrium.

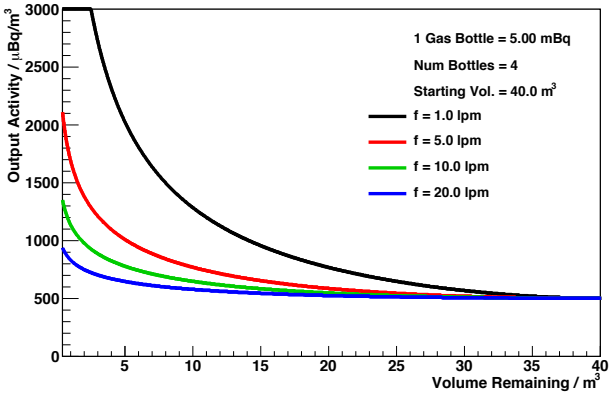

Figure 7.1: Specific activity of four cylinders, each 50 litres in volume, as a function of the volume remaining. A combined activity of 20 mBq is used for radon emanation with a starting gas volume of 40 m^3.

For SuperNEMO tracker measurements only flow rates between $7 - 14$ lpm are used with full cylinders and no more than 60% of the total volume of gas used, hence the output activity is approximately uniform over time.

7.1.2 Measuring Full Cylinders

The experimental procedure is to first heat then clear the trap of any residual radon, then cool the trap to - 45 C. Once cooled, flow the sample gas through the trap to exhaust for $\sim$ 20 hours then seal the trap. Finally, the trap is heated and the radon transferred to the detector for measurement. A typical measurement of a nitrogen cylinder is shown in Figure 7.2b.

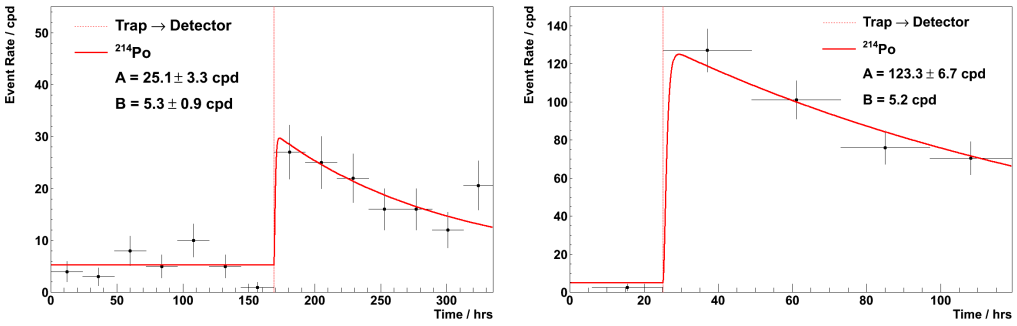

(a) Line Only **(b)** Line and Gas

Figure 7.2: (a) ^{214}Po activity of both supply line and 0.075 m^3 of helium. (b) ^{214}Po activity of both line and 10.7 m^3 of nitrogen.

The activity of radon in the detector immediately after transfer from the trap is given by

$$A_D = \epsilon_{tr} A_C \left(1 - e^{-\lambda T_C}\right) + \epsilon_{tr} \left(\epsilon_T \left(T_f\right) A_G + \frac{\epsilon_T \left(T_f\right) f a_G}{\lambda}\right) \left(1 - e^{-\lambda T_f}\right) e^{-\lambda T_{trans}} \tag{7.2}$$

where ϵ_{tr} is the transfer efficiency, ϵ_T is the trapping efficiency, A_C is the intrinsic activity of the RnCL carbon trap, A_G is the activity of the gas line and a_G is the specific activity of gas from cylinders [60]. The relevant timings for this measurement are as follows

- T_C: time between clearing the trap and detector transfer (1605 min).
- T_f: time that the line is in contact with the trap (1200 min).
- T_{trans}: time between stopping collection and detector transfer (135 min).

The measurement shown in Figure 7.2b produced a result of 4.53 ± 0.25 mBq with $T_C = 1462$ min, $T_F = 1070$ min and $T_{trans} = 128$ min. Applying the trapping and transfer efficiencies found from the flow-through calibration in Section 6.4, the specific radon activity of the gas is extracted as 957 ± 132 µBq/m^3. This translates to a mean intrinsic activity per bottle of 9.6 mBq.

The same measurement but with helium cylinders produced a result of 77 ± 13 µBq/m^3, resulting in a mean intrinsic activity per bottle of 0.8 mBq. The difference between the intrinsic activity of helium and nitrogen cylinders is surprising as the supplier

states they are made from similar materials. It could be as a result of natural variation in the contamination of the steel used in producing the helium and nitrogen cylinders.

Several more cylinders of nitrogen and helium were measured to determine the variation of radon activity between cylinders. The results showed large variation between different batches of cylinders from the same supplier, as shown in Table 7.1. Since the carrier gas contributes to the largest background during a tracker measurement it is critical the cylinders used would have to be measured separately in order to find the activity of the carrier gas to be subtracted from the measured result. This doubles the time required for each tracker measurement as well as introduces large uncertainties resulting from extrapolation of radon levels of the carrier gas.

7.1.3 Cylinder Gas Activity Effects On MDA

The large and variable radon content of the carrier gas can impact the MDA achievable by the RnCL. A plot of the RnCL MDA as a function of the carrier gas activity is shown in Figure 7.3. It can be seen in order to achieve better than 0.15 mBq/m^3 of sensitivity the activity of the supply gas must not exceed 1.5 mBq/m^3.

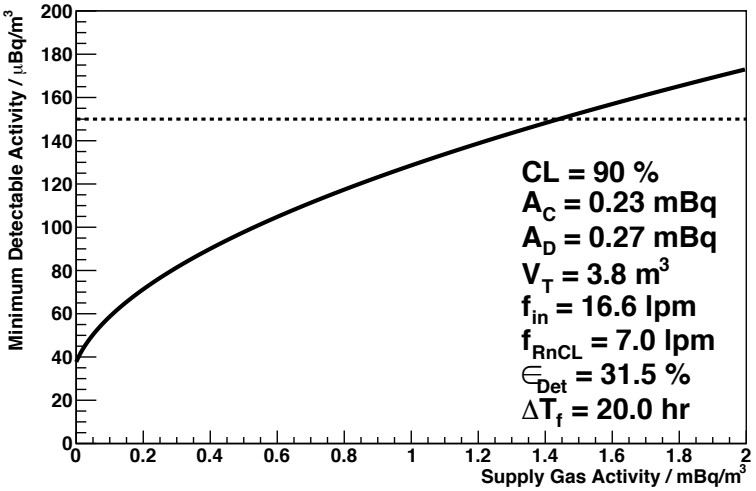

Figure 7.3: Sensitivty of the RnCL for a C-section measurement as a function of the input gas activity.

7.2 Gas Purification System

A gas purification system (GPS) was devised and constructed which is able to suppress the radon activity in a carrier gas. The system was developed to remove one of the greatest sources of systematic uncertainties as a result of the relatively high content and variability of radon in N_2.

The radon trap system was designed and built at CPPM [61] which was estimated to suppress radon by a factor 10 for nitrogen and 5×10^{10} for helium. A design schematic is shown in Figure 7.4, which essentially consists of two freezers operated at temperatures of -50 C and -80 C containing 1.5 kg and 0.5 kg of activated charcoal each respectively.

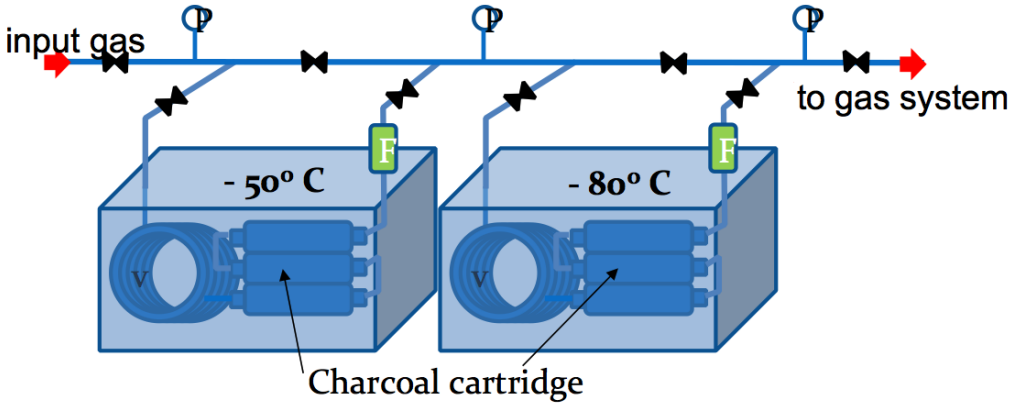

Figure 7.4: Schematic of the GPS developed at CPPM.

The system works by passing the carrier gas through the activated charcoal where radon is adsorbed. The low temperature improves the radon capture efficiency of the charcoal, housed in stainless steel cartridges that can be replaced if necessary. The GPS was delivered to MSSL and installed in May 2014. The temperature was monitored regularly to ensure it remains stable.

7.2.1 Background Measurement

The first measurement carried out after installation was the background of the GPS itself. The GPS was thoroughly flushed using helium to ensure any residual air was replaced with helium. It was then left to emanate immersed in helium under atmospheric pressure.

The system was left for 21 days to allow any residual radon to decay away and the radon level inside the trap to reach an equilibrium. The gas inside the GPS was

then transferred into the radon detector for measurement. The resultant activity measurement is shown in Figure 7.5.

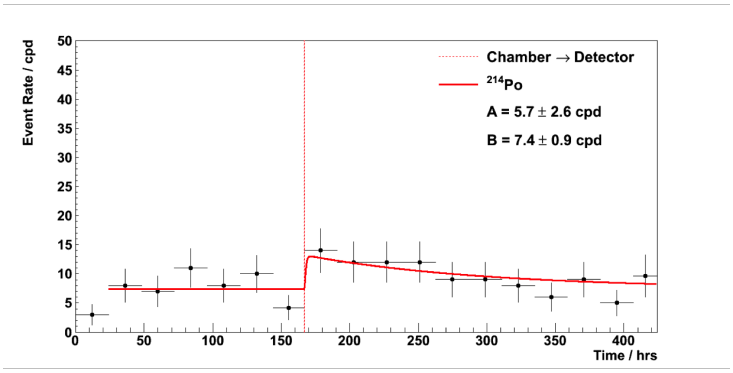

Figure 7.5: Result from the measurement background activity of the GPS after 21 days of emanation time.

From this result a contribution of 1.6 ± 0.7 cpd of background can be expected from the GPS over a 24 hour trapping and transfer measurement period.

7.2.2 Radon Suppression Measurement

In order to verify the GPS suppression of radon in carrier gases a measurement was carried out on 4 full cylinders of zero grade nitrogen. The procedure for this measurement is similar to that of a c-section measurement. Details of previous c-section and gas cylinder measurements have been documented [62].

1. The trap is heated to above 200 °C to clear it of any residual radon.

2. Once the trap is cooled to below -40 °C start to flow the sample gas, first through the GPS, then through the RnCL trap and out to exhaust at 7 lpm for 20 hours.

3. Seal the trap and heat to above 200 °C. Once the necessary temperature is reached, transfer the gas, using helium as the carrier gas to improve efficiency, into the radon detector for measurement.

The resultant measurement of gas activity is shown in Figure 7.6.

The activity of radon in the detector immediately after transfer from the trap is calculated using (7.2). The relevant timings for this measurement are as follows

- T_C: time between clearing the trap and detector transfer (1605 min).
- T_f: time that the line is in contact with the trap (1200 min).

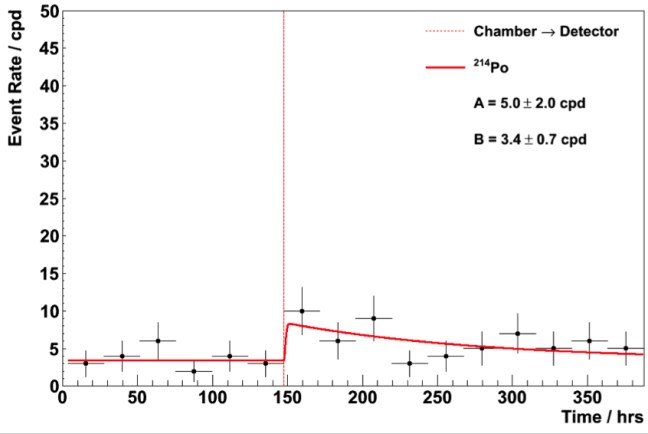

Figure 7.6: Result from the measurement of radon content in zero grade cylindered nitrogen.

- T_{trans}: time between stopping collection and detector transfer (135 min).

Using the trapping and transfer efficiencies from the flow-through calibration shown previously, the specific activity of the nitrogen gas, a_G can be extracted as 20 ± 13 μBq/m^3. This can be compared to previous measurements of cylindered and boil-off gas as shown in Table 7.1.

Gas	Source	Radon Level (μ Bq/m^3)
He	Cylinder	70-100
N_2	Cylinder	400-1000
N_2	Boil-off	90-140
N_2	GPS	20

Table 7.1: Radon activity measured from various carrier gas and containers.

Comparing the radon activity of cylindered nitrogen before and after it passes through the GPS, a suppression factor of 20 can be conservatively estimated.

7.3 Gas System Measurements

The gas system was designed and built at UCL to deliver the required gas mixture directly into the demonstrator. Since the gas mixture contains 4% ethanol, any

radon emanated by the gas system cannot be filtered using a carbon trap, therefore, the radon would contribute directly to the demonstrator radon budget. Hence it was essential to test it for radon emanation. Three different tests were devised to measure the radon emanation of the gas system; a flow through measurement, spike measurement and finally a RnCL measurement.

The gas system has already been used for commissioning the completed quarter trackers using the operational gas mixture. The high content of ethanol present would contaminate the RnCL carbon trap by significantly reducing its trapping efficiency, rendering any measurement data indiscernible. Even if it was possible to calibrate the trap for reduction of trapping efficiency as a function of ethanol, the small carbon trap would be quickly saturated by the ethanol which would severely reduce the volume of gas measurable which is directly related to the sensitivity achievable. The ethanol would also cause deionisation of the radon decay daughters hence greatly reducing the detection efficiency of the electrostatic radon detector. This could again be calibrated however even a few ppm of ethanol can cause the detection efficiency to halve.

7.3.1 Ethanol Removal

It was decided the best way to disentangle the radon emanation from the gas system would be to drain the ethanol completely. This would essentially turn the gas system into a similar setup as the radon emanation chamber described above.

Although it is possible to quickly drain the main chamber of ethanol, for the RnCL measurement, the level of ethanol within the output gas has to be at a level below 10 ppm. A residual gas analyser was acquired to monitor the content of the gas system exhaust before and after it was drained of ethanol. The ambient cleanroom air was measured along with the ethanol content set to 1-4% to calibrate the residual gas analyser.

After the main chamber was drained, 150 m^3 of standard grade cylindered nitrogen was flushed through the gas system at a flow rate of 10 lpm and the exhaust was continually monitored to track the reduction in ethanol levels. After 10 days of flushing, the ethanol levels in the gas stabilised at 6 ppm. This level was higher than expected and likely due to the fact standard grade cylindered nitrogen contains trace amounts of impurities which could contribute to the observed levels of ethanol.

To establish if this was indeed the cause the gas system was flushed with a higher purity nitrogen which has known levels of contamination, 2000 ppm of oxygen, CO, CO_2, hydrocarbons, hydrogen and water. The levels of observed ethanol did drop to 5 ppm but once again plateaued.

A third flushing attempt was performed using a cleaner, higher purity helium containing 700 ppm of O, 200 ppm of water, 100 ppm of CO, CO2, hydrocarbons and hydrogen. The ethanol content again dropped and stabilised at 4 ppm, the remaining observed ethanol was likely as a result of the impurities from the gas itself instead of contribution from the gas system. However, this could not be verified.

7.3.2 Flow Through Measurement

The flow through measurement requires the carrier gas to pass directly through the electrostatic radon detector which is in situ taking data. The gas system was setup to flow at 4.2 slpm instead of the nominal 14 lpm to increase the sensitivity of this measurement.

The gas system was purged using zero grade nitrogen 24 hours prior to the start of the measurement. The nitrogen was then replaced with zero grade helium which improves detection efficiency of the detector. The helium was flowed through the gas system, the electrostatic detector and finally to exhaust. This was carried out over 3 days and the resultant plots are shown in Figure 7.7.

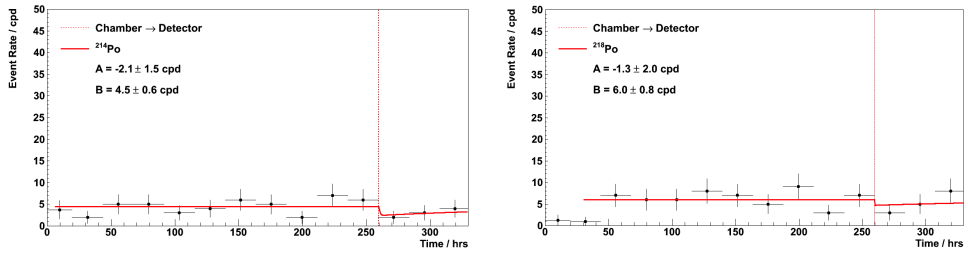

(a) ^{214}Po Rate. **(b)** ^{218}Po Rate.

Figure 7.7: Activity from the flow through measurement of the gas system.

To extract a limit from this measurement the suppression factor due to the gas flow must first be taken into account. This can be calculated as;

$$A_D = \frac{A_0}{1 + \frac{\phi}{\lambda V}} + A_B \tag{7.3}$$

where

- A_D is the detected activity
- A_0 is the true activity

- A_B is the intrinsic detector background activity
- ϕ is the flowrate
- λ is the decay constant for radon
- V is the volume (combining the gas system, 50 litres, and the radon detector, 70 litres)

From a flow rate, ϕ, of 4.2 lpm and a volume, V, of 120 litres a suppression factor of 280 can be calculated. Taking this into account, a limit can be set at < 25 mBq at 90% CL. This confirms there are no major radon emitter inside the gas system. This measurement allowed further purging of the pipework of any residual ethanol.

7.3.3 Spike Measurement

The setup for this measurement is similar to that of a radon emanation chamber measurement. The gas system is treated as essentially an large emanation chamber. Due to it's volume, the gas cannot be transferred in its entirety to the radon detector for measurement without creating a large overpressure inside the electrostatic detector. Such overpressure can effect the detection efficiency as well as putting pressure on the detector seals.

To begin, the gas system was purged using zero grade helium which had been further purified using the GPS. The system was then sealed to allow for emanation at atmospheric pressure. After the emanation period, and immediately prior to gas transfer the gas lines before and after the sealed system were flushed in order remove any possible background contribution.

The transfer was done by flowing 25 litres of helium into the gas system which displaces 25 litres of gas into the electrostatic detector for measurement. The detector is sealed and the results are shown in Figure 7.8, which corresponds to an activity of 1.97 ± 0.31 mBq. The observed difference in activity of ^{214}Po and ^{218}Po could be due to trace levels of ethanol affecting the detection efficiency, even at less than 10 ppm levels.

7.3.4 RnCL Measurement

The setup for this measurement requires the gas system to be purged continuously for 50 hours prior to starting the trapping. This ensures the radon level inside the gas system reaches an equilibrium state. After purging, the gas is flowed at a constant rate through the RnCL carbon trap which has been cooled to -35 °C . After 20 hours of trapping, a total gas volume of 10 m^3 was sampled. The carbon trap is

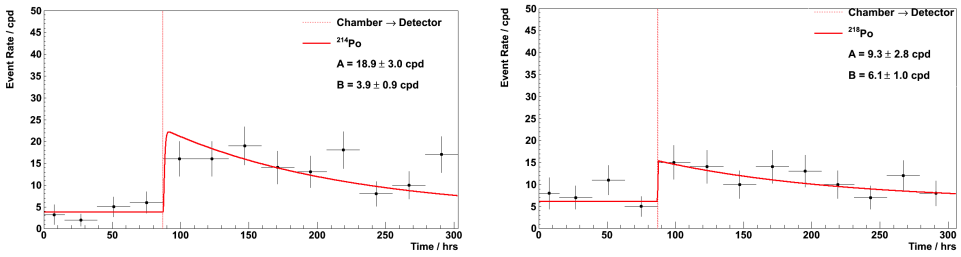

(a) ^{214}Po Rate. **(b)** ^{218}Po Rate.

Figure 7.8: Activity from the spike measurement of the gas system.

then sealed and heated to 200 °C before the gas is transferred from the trap into the detector using 25 litres of helium.

The detector is sealed and the results are shown in Figure 7.9.

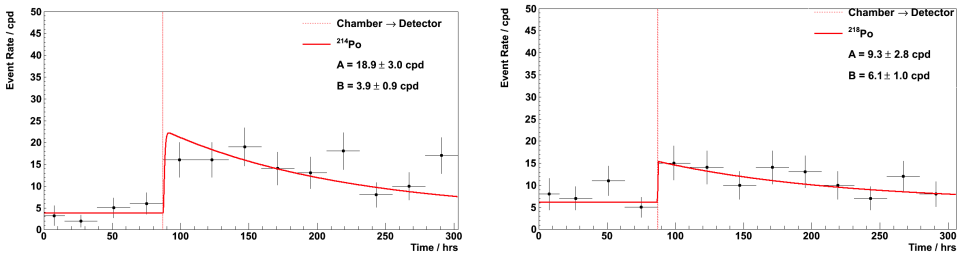

(a) ^{214}Po Rate. **(b)** ^{218}Po Rate.

Figure 7.9: Activity from the RnCL measurement of the gas system.

A model is created where radon activity emanates uniformly within the gas system and is passed into the detector as a result. The number of radon atoms inside the gas system, N_G, can be found by considering emanation and atomic decay within the gas system and those that are extracted by the gas flow:

$$\frac{dN_G}{dt} = A_G - \lambda N_G - \frac{fN_G}{V_G} \tag{7.4}$$

where, A_G is the intrinsic ^{222}Rn activity of the gas system, λ is the radon decay constant, f is the gas flow rate and V_G is the volume of the gas system. Under operational conditions, the radon activity inside the gas system will be in equilibrium,

so that N_G is given by

$$N_G = \frac{A_G}{\lambda + \frac{f}{V_G}} = \frac{A_G V_G}{\lambda V_G + f} \approx \frac{A_G V_G}{f} \tag{7.5}$$

where the final approximation is very good since it is expected that $\lambda V_G \sim O(10^{-3})$ m^3/hr and $f \sim O(1)$ m^3/hr. Using this an activity of xxx was found which is in agreement with the result of the spike measurement.

7.4 Tracker Measurements

The RnCL has been shown to be able to measure a supply of gas, of uniform activity, at a sensitivity below the SuperNEMO radon requirement. This is important since the main quantity the RnCL must be able to verify is the SuperNEMO tracker has achieved a radon emanation level <0.15 mBq/m^3. The tracker for the demonstrator module is composed of four segments each in the shape of a C, hence frequently referred to as c-sections. Each individual tracker section is constructed at MSSL where it must then be sealed and tested for radon emanation before being transported to the LSM for assembly Figure 7.10, In total each quarter tracker is composed of a stainless steel frame, x number of x-wall and x number veto PMTs. There are x number of cells inserted as cassettes of 18 cells at a time.

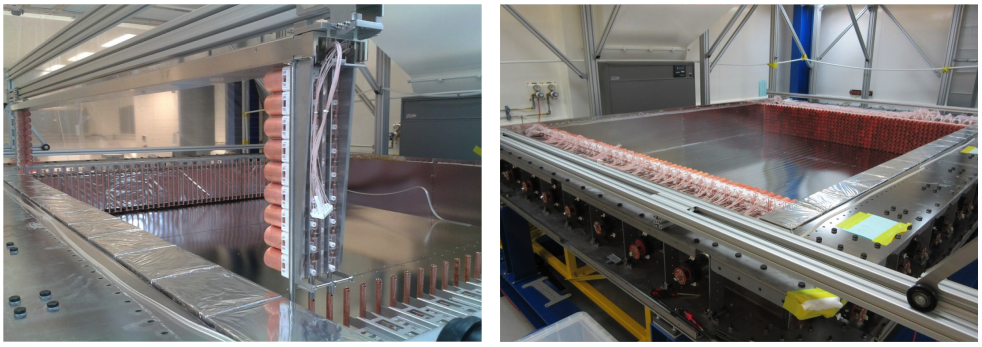

(a) Single cassette installation. **(b)** Complete quarter tracker.

Figure 7.10: Quarter tracker construction inside the MSSL cleanroom.

The first two C-Sections were measured; before the tracking cell are inserted, half way through cell insertion and, finally, measured again after construction was complete. This provided the necessary information to disentangle any source of radon emanation so it might be pin pointed and removed.

Prior to full Demonstrator assembly the C-section must be sealed without the calorimeter walls to enable radon testing and commissioning of the tracker cells. Customised gas-sealing plates were designed, which are fixed in place of the calorimeter wall, source foil and the point at which two C-Sections are joint together.

7.4.1 Measurement Starting Point

In an ideal scenario the C-section would be left perfectly sealed for an extended period prior to the measurement in order to allow for the radon build up. However, in reality, a C-section is not a sealed unit as it has small leaks. These leaks means that it must retain a constant small overpressure to prevent environmental radon from diffusing inside. The number of radon atoms inside a C-section, N_T can be modelled by:

$$\frac{dN_T}{dt} = A_T + A_G - \lambda N_T - \frac{f_{in} N_T}{V_T} + \frac{f_{in} a_G}{\lambda} \tag{7.6}$$

where A_T and A_G are the intrinsic activity of the C-Section and gas supply line respectively, f_{in} is the input flow rate of gas, $V_T = 3.8$ m^3 is the volume of one C-section and a_G is the activity of gas per unit volume.

Since the C-Section was exposed to the cleanroom air prior to being sealed and the seal is not perfect it is expected some residual radon from the atmosphere is housed inside detector components, as indicated from the radon harbouring hypothesis, shown in Section 6.3.3. Therefore, after the C-Section is sealed it must be kept under a constant overpressure by actively purging with cylindered nitrogen at 3 lpm, creating an overpressure of 2 mBar inside the tracker for 18 days before a measurement can be carried out.

7.4.2 The Anti Radon Tent

To isolate the each tracker module from the environment, whilst the C-Section is kept under purge, an anti radon tent was devised which will surround the C-Section and be purged constantly with pure nitrogen. Several designs for the tent were trialled, with the final design being made from large double layered polyethylene sheets heat sealed together. The tent is then draped over each C-Section and sealed securely to the floor. Four flushing points were fitted to the tent, equally spaced apart, and purged at a rate of 3.6 m^3/hr. A clear overpressure is established within the tent as can be seen by the clear bulge of the tent both above and around the C-Section, as shown in Figure 7.11.

A RAD7 was used to confirm and monitor the reduced radon levels inside the tent at all times during a C-Section measurement. The radon levels of the cleanroom

Figure 7.11: Photograph of the anti-radon tent covering the C-section.

was monitored closely and varies from $2 - 3$ mBq/m^3 to $20 - 30$ mBq/m^3. This compared to the radon level measured inside the anti radon tent of < 0.1 mBq/m^3 shows a reduction by more than 2 orders of magnitude, shown in Figure 7.17a. Since the tent is purged with cylindered nitrogen there was also a visible reduction in the humidity levels inside the tent as shown in Figure 7.17b. The tent was used for each C-Section radon emanation measurement.

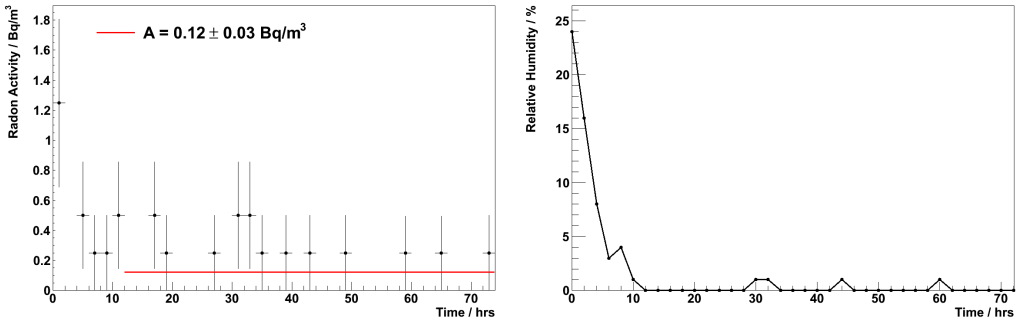

(a) Radon Activity **(b)** Humidity

Figure 7.12: Measurements made by the RAD7 device inside the anti-radon tent during a C-section measurement. Radon activity and humidity measurements are shown.

7.4.3 Measurement Procedure

For the C-Section measurement the RnCL was connected to the C-Section as shown in the schematic in Figure 7.17b. The connections were made using 2 mm thick nylon pipes which were tested for radon emanation and showed no excess contribution. Due to the low overpressure inside the C-Section, a diaphragm pump was attached at the exhaust of the RnCL in order to achieve sufficient flow rate for measurement.

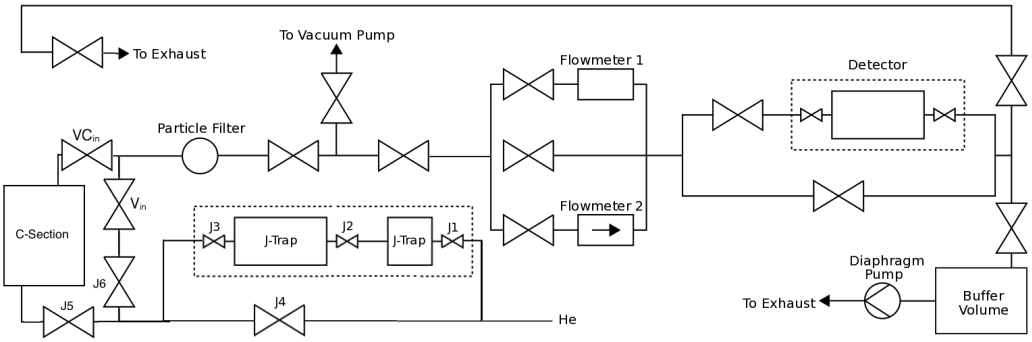

Figure 7.13: System setup for a c-section measurement.

Before the start of a measurement, the flushing rate into the C-Section is increased from the purging of 3 lpm to 14 lpm. This flow rate was chosen to maximise gas flow through the RnCL whilst maintaining a healthy overpressure inside the tracker module. The output activity of the gas from the tracker can be modelled as:

$$A(t) = \frac{A_T + A_G + f_{in} a_G/\lambda}{\lambda'_T/\lambda}\left(1 - e^{-\lambda'_T t}\right) + A_0 e^{-\lambda'_T t} \tag{7.7}$$

where A_0 is the measured activity and

$$\lambda'_T = \lambda + \frac{f_{in}}{V_T} \tag{7.8}$$

It can be seen from Figure 7.14 that after 50 hours the output activity reaches an equilibrium even with high intrinsic activities. Therefore, each C-Section was flushed at 14 lpm 50 hours prior to the start of a measurement with 7 lpm going through the RnCL and the rest exhausted through leaks.

After 50 hours the trap on the RnCL is heared to clear it of any residual radon, setting time zero of T_C. Once the trap is cleared it is sealed under atmospheric pressure and cooled to - 35 °C. Once the trap is cooled, the nitrogen from the C-Section is diverted through the trap, at 7 lpm, and out to exhaust. After 20 hours the trap is again sealed under atmospheric pressure and allowed to warm. Finally, the

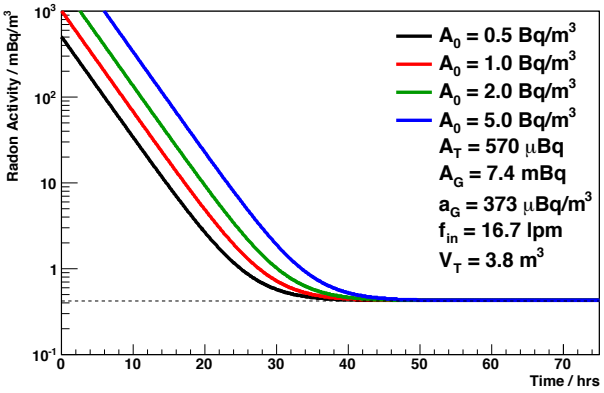

Figure 7.14: Activity inside the C-section whilst flushing prior to a radon measurement, as modelled by Equation (7.7).

trap is heated to 220 °C before the gas inside is transferred into the radon detector for measurement.

7.4.4 C-section Activity Calculation

Since each C-Section is not perfectly sealed and radon is lost through the leaks modelling is required to extract the intrinsic radon activity of the C-section from background components. Before starting any measurement the C-section is flushed at $\sim$ 14 lpm for 50 hr. At this point, the equilibrium activity, a_T^{eq}, inside the C-section is given by:

$$a_T^{eq} = \frac{A_T + A_G + f_{in}a_G/\lambda}{V_T + f_{in}/\lambda} \tag{7.9}$$

The specific activity, A_T, of the C-Section can be extracted by rearranging Equation (7.9) to give:

$$A_T = \left(1 + \frac{f_{in}}{\lambda V_T}\right) V_T a_T^{eq} - A_G - \frac{f_{in}a_G}{\lambda} \tag{7.10}$$

7.4.5 Background Measurement

In order to better estimate the background radon contribution during a C-Section measurement a "blank" measurement was carried out. This measurement has the same setup as the gas cylinder measurement but with the addition of 60 meters of gas line used during C-Section radon measurements. A total volume of 6.73 m^3 was

used producing a result of:

$$a_G^{used} = 0.044 \pm 0.015 mBq/m^3 \tag{7.11}$$

The cylinders used where only half full as compared to the start of C-Section measurements with a starting pressure of 90 bar instead of 180 bars, as used during C-Section measurements. Therefore, the specific activity of the gas with a full cylinder can be estimated using:

$$A(T_2) = \left(1 - e^{-\lambda(T_2 - T_1)} + \frac{V(T_1)}{V(0)} e^{-\lambda(T_2 - T_1)}\right) A_B \tag{7.12}$$

The resulting specific activity of the nitrogen was:

$$a_G = 23 \pm 8 \text{ µBq/m}^3 \tag{7.13}$$

This result is in good agreement with previously measured gas activity after passing through the GPS.

7.4.6 C-Section Measurement Results

The results from the measurements of each C-Section are presented here. For each test the setup was identical with the C-Section enclosed by the gas sealing plates and then tested for gas tightness. The sealed C-Section is then enclosed within the anti radon tent where it is purged continuously for 18 days prior to a measurement.

First Quarter Tracker

The result from the measurement of the first fully populated C-Section, C0, is shown in Figure 7.15. From this result, a_T^{eq} was calculated to be 0.118 ± 0.018 mBq/m^3 which translates to a specific activity of:

$$A_T = 11.37 \pm 1.44 mBq = 2.99 \pm 0.38 mBq/m^3 \tag{7.14}$$

Second Quarter Tracker

The result from the measurement of the fully populated C1, is shown in Figure 7.15. From this result, a_T^{eq} was calculated to be 0.118 ± 0.018 mBq/m^3 which translates to a specific activity of:

$$A_T = 15.26^{+2.50}_{-3.82} mBq = 4.02^{+0.66}_{-1.01} mBq/m^3 \tag{7.15}$$

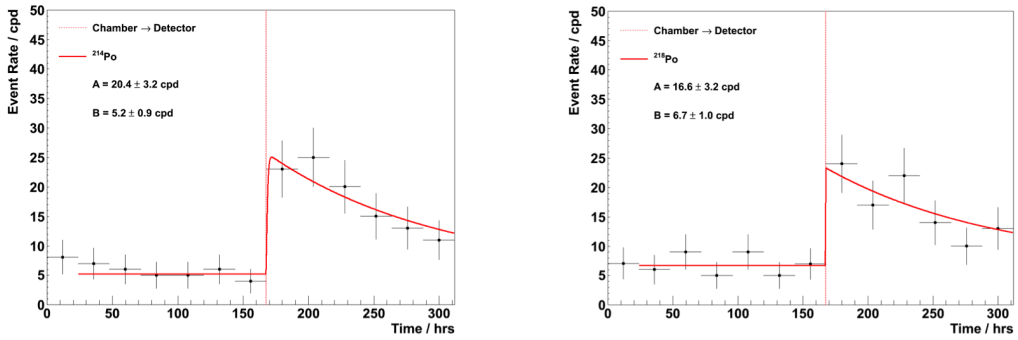

(a) Radon Activity **(b)** Humidity

Figure 7.15: Result from the RnCL measurement of C0.

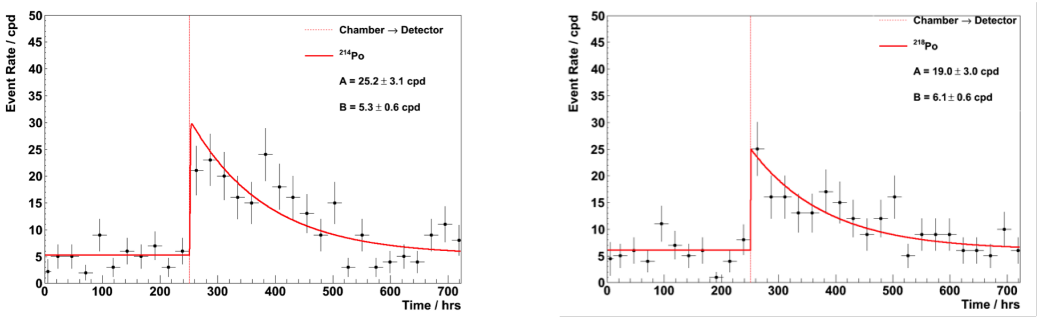

(a) Radon Activity **(b)** Humidity

Figure 7.16: Result from the RnCL measurement of C1.

Third Quarter Tracker

During the construction of C0 and C1, radon emanation measurements of a tracker component showed positive contribution to the tracker gas. This component was replaced for the construction of C2. From emanation results the contaminated component was estimated to contribute an activity of 4 ± 1 mBq per C-Section.

The result from the measurement of the fully populated C2, is shown in Figure 7.15. As expected the radon level for C2 was reduced. From this result, a_T^{eq} was calculated to be 0.118 ± 0.018 mBq/m^3 which translates to a specific activity of:

$$A_T = 4.36 \pm 1.31 mBq = 1.15 \pm 0.34 mBq/m^3 \tag{7.16}$$

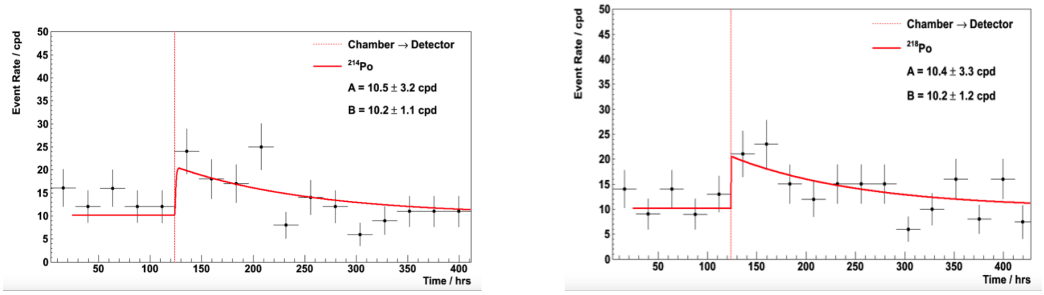

(a) Radon Activity **(b)** Humidity

Figure 7.17: Result from the RnCL measurement of C2.

Summary

The result from radon activity measurements of the first three C-Sections of the SuperNEMO Demonstrator are shown in Table 7.2.

	C0	C1	C2	C3 (Estimate)
Activity (mBq)	11.37 ± 1.44	$15.26^{+2.50}_{-3.82}$	4.36 ± 1.31	10.33

Table 7.2: Summary of C-Section radon measurement results. The estimated figure for C3 is based on the average measured value of C0-2.

Taking the radon emanation value for the fully populated C-Sections and extrapolating it to the final Demonstrator module would result in an activity of:

$$A = 41.3 \pm 4.7 mBq = 2.7 \pm 0.31 mBq/m^3 \tag{7.17}$$

If the Demonstrator were to apply a flushing rate of $2m^3$ per hour then the radon activity should be suppressed by a factor 18.4 which would result in a specific activity inside the tracker gas of < 0.15 mBq/m^3, thus achieving the SuperNEMO target.

Chapter 8

Gamma Ray Spectroscopy at Boulby Underground Laboratory

"Anyone who lives within their means suffers from a lack of imagination."

- Oscar Wilde

Gamma ray spectroscopy is essential for determination of nuclear contamination. The ideal detector for gamma ray spectroscopy would have excellent;

- Detection efficiency (large Z for high absorption coefficient);
- Resolution (accurate measurement of energy deposited);
- Stability (over time, temperature, pressure etc);
- Readout (easy access to signal);
- Background (as low as possible);

In practice, the parameters would have to be compromised to build the most optimal detectors at a feasible cost and size. The most commonly used method for gamma ray spectroscopy is using a semi conductor material as the target. The choosen semi conductor should fulfil as many of the ideal detector criteria as possible.

Silicon is a good candidate as it is readily available in a high purity form at a reasonable cost. However, it has a low Z which means it is impractical to construct a gamma-ray detector from it. Instead it is often used for measurement of low energy photons and X-ray spectroscopy.

Other potential candidates include mercuric iodide (HgI_2), cadmium telluride (CdTe) and cadmium zinc telluride (CdZnTe) which have relatively high Z, hence large absorption coefficients, and larger band gap so they can be operated at room

temperature. However, developments need to be made to create larger crystals of high purity. More fundamentally the charge carrier mobilities of these semi conductors are relatively low, especially the mobility of holes are much lower than electrons. This makes the materials susceptible to trapping and imposes severe charge collection problems on distances over 1 mm which limits detector size. Progress has been made to enhance the charge collection efficiency of cadmium telluride and cadmium zinc telluride detectors using improved electronics but presently they remain small detectors. Another potential future detector candidate could be gallium arsenide.

In reality there is one semiconductor material which best fits all the requirements, that is germanium. It has a relatively high Z, suitably large crystals, can be made at reasonable costs to a very high purity and crystal perfection. The charge carrier mobility is more than an order of magnitude better than HgI_2, CdTe and CdZnTe, in particular for holes which is more than 2 order of magnitude higher. For good energy resolution, the semiconductor material should produce as many electron-hole pairs as possible per unit energy deposited;

$$n = \frac{E_{abs}}{\varepsilon} \tag{8.1}$$

where n is the number of electron-hole pairs produced, E_{abs} is the absorbed gamma energy and ε is the average energy needed for electron-hole pair creation. Germanium has the lowest ε of all the semiconductor materials described here. The only disadvantage of germanium is the low band gap. Hence, germanium detectors must be cooled in order to reduce thermal generation of charge carriers, otherwise the energy resolution is washed out by leakage current induced noise.

A new low background germanium facility has been established at the Boulby Underground Laboratory, located in the North East coast of England. It is located within a working potash and rock salt mine, the deepest in the UK at 1070 metres (2805 m w.e.) below ground [63]. The air inside the laboratory has a naturally low level of radon content due to the low levels of uranium and thorium in the surrounding salt tunnel. At the start of this PhD project, a single germanium detector was resurrected for material screening purposes. Since then the single detector has been completely refurbished, replacing all components except for the high purity germanium crystal. Three more new low background germanium detectors have also joined it's ranks with customised shielding constructed for each detector. The four detectors are now housed in a dedicated gamma-ray spectroscopy suite, which is maintained as a class 1000 cleanroom. Several other detectors are planned to be established at Boulby over the next year, moving Boulby to become a world class germanium measurement facility.

8.1 Germanium Detectors

Germanium detectors are semiconductor diodes with a p-i-n structure in which the intrinsic (i) region is sensitive to ionisation radiation, particularly x-rays and gamma rays. Germanium doped with five valent impurities will have one excess electron at the impurity lattice site. Such impurities are known as donor impurities and will introduce donor states just below the conduction band, such germanium is called n-type germanium ('n' for negative donor impurities). Therefore, germanium doped with three valent impurities have one too few electron. Such impurities are known as acceptor impurities which introduce acceptor states just above the valence band. Germanium doped with such impurities is called p-type germanium ('p' for positive acceptor impurities).

High purity germanium (HPGe) detectors are typically constructed using a block of high purity p-type germanium with an n+ layer on one face, shown in Figure 8.1. When a reverse bias is applied to the detector, a depletion layer is then created throughout the p-type material. Interaction of gamma-rays with material inside the depleted volume creates charge carriers (electrons and holes) which migrate to the p and n electrodes as a result of the electric field.

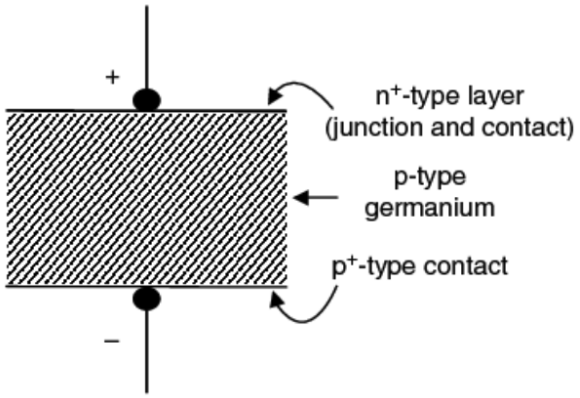

Figure 8.1: The layout of a p-type germanium detector.

8.1.1 Types of Germanium detectors

There are a number of different configurations of germanium detectors optimised depending on application. The standard geometries and their detection efficiencies over the energy range 0-1000 keV are shown in Figure 8.2. The detection efficiency curves show are only indicative, actual efficiency depends on the exact geometry of the Ge crystal and the sample used for measurement.

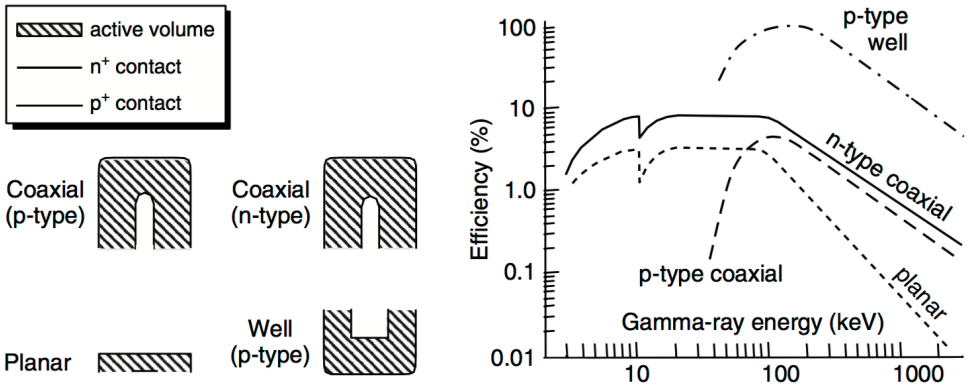

Figure 8.2: The 4 standard detector configurations and an indication of efficiency for each geometry.

At low energies the efficiency is limited due to the absorption of gamma-rays by various detector components before they reach the Ge crystal. At high energies, the efficiency is limited by the Ge crystal size and the drop in absorption coefficient as energies increase. Modern Ge detectors with large crystals are capable of measurement up to more than 10 MeV.

8.1.2 Detector schematic

Typical HPGe detectors are very sensitive to any external gamma-rays and need to be shielded in order to achieve suitable background levels for low activity material measurements. Ideally the shielding would be made of a material of high atomic number and low intrinsic activity. There are many factors to consider when building a castle to house HPGe detectors;

- Lead is usually the most popular choice of shielding against external gammas. For general purposes 50 mm of lead wall on all sides should be sufficient ideally using interlocking bricks to prevent any gaps which can offer a line of sight for gammas. There are many different grades of lead which have varying levels of radioactivity. Fresh mined lead is usually more radioactive because although uranium and thorium are removed in the processing of lead, ^{210}Pb with its high half-life, 22.3 years, remains which undergoes beta decays hence emitting gamma and Bremsstrahlung effecting high sensitivity detectors. Certified low activity lead, <50 Bq/kg, can be purchased at increased cost and archeological lead from sunken roman ships offer lead of even greater radio-purity, as the water shields the lead from cosmic rays and man-made isotopes.

- Oxygen free high conductivity (OFHC) copper is often used as the core shielding, as the process to remove oxygen also eliminates other radioactive contaminates. However, it is expensive and has a high cross section for thermal neutron capture and for the cosmogenic production of radioactive nuclei.
- Cadmium was also used as an internal shielding, however due to its extremely high toxicity it is no longer applied.
- Steel can be used, however it can contain high levels of ^{60}Co.
- Aluminium is sometimes used as internal lining, however it usually contains uranium and thorium so should not be used for extremely low background detections.
- Mercury would also make excellent shielding as it can be readily purified via distillation. However, it is expensive, difficult to contain and shares similar issue of toxicity as cadmium.

There is no single perfect design for HPGe shielding, it depends on background requirements and costs. A standard configuration usually involves 50 - 100 mm of lead followed by 20 - 100 mm of copper all surrounded by an anti-radon tent, as shown in Figure 8.3. The copper is essential to remove low energy gammas and fluorescent x-rays in the background spectra. If using roman lead or a combination of cheap lead with a inner lining of roman lead then less copper is required.

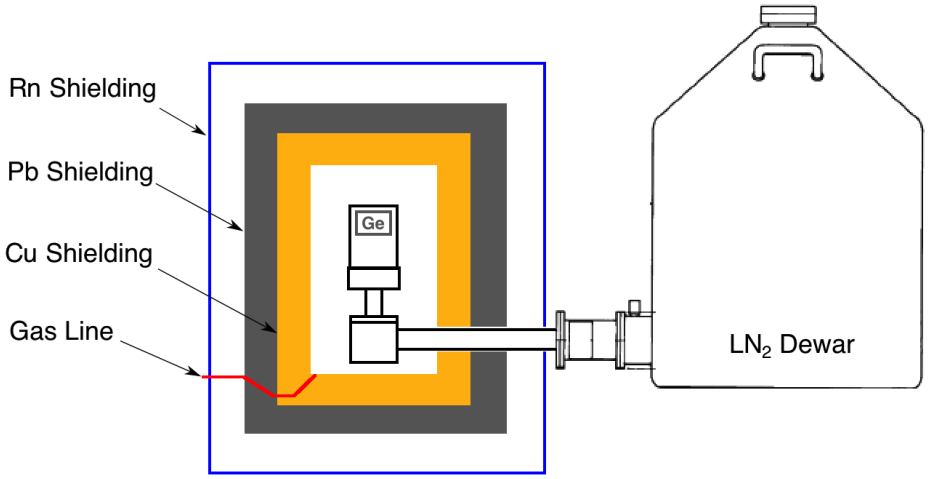

Figure 8.3: Typical HPGe detector schematic, the crystal is mounted inside a vacuum endcap and cooled using a cold finger which is in thermal contact with a liquid nitrogen dewar.

The detector shielding should also be configured to allow for a large sample capacity. Keeping a large distance between the end cap and the castle wall to create the large capacity also has the added benefit of minimising the effects of backscattering which can contribute to the background spectra. The detector end cap is usually made of either magnesium or carbon fibre 0.9-1 mm in thickness and extremely radio-pure.

The Boulby detector castles were designed with 100 mm of lead, selected through screening to have the lowest ^{210}Pb content and has been underground for more than 20 years. This lead shielding is followed by 100 mm of high-purity copper which is used to reduce the remaining ^{210}Pb gammas, ^{210}Bi bremsstrahlung as well as the fluorescent X-rays from the lead. In order to remove electronic noise, the detector and the cryostat were kept electrically isolated from the shielding by inserting insulation around the stem of the detector. For radio-purity purposes the preamplifier is also placed outside the detector shielding.

The copper layer was cleaned using diluted acidic solution to remove any residual surface contamination then wiped down using deionised water before installation. The surface contaminates which were remove include residual ^{210}Pb from radon decay daughters which plate out on exposed surfaces. Also, as Boulby is located inside an active salt mine, there was a significant level of contamination from dust brought into the lab which contains ^{40}K, ^{238}U and ^{232}Th. The lead was cleaned using an alkaline solution to again remove dust contaminations on the surface and was then wiped down using IPA before reassembly.

8.2 Detector Calibration

There are three main calibrations required in order to interpret the gamma-ray spectrums obtained by the Ge detector in terms of measured activity;

- Energy calibration - to convert from ADC to energy;
- Resolution calibration - to determine the variation of peak width as a function of energy;
- Efficiency calibration - the ratio of counts observed to number of decays as a function of energy.

The detector is calibrated regularly with radioactive sources such as ^{137}Cs, ^{60}Co, ^{57}Co and a Multi-Gamma Source (MGS) containing ^{65}Zn and ^{155}Eu. The MGS activity is known and is certified by Canberra to within 5% accuracy. An IAEA source is also used with isotope activities known to better than 1% accuracy [64].

8.2.1 Energy Calibration

The raw data is recorded using a 13 bit ADC which is used in conjunction with the amplifier and a multichannel analyser (MCA) to generate a 8192 bin spectrum. This can be converted to energy by taking spectrums of known gamma sources, such as ^{60}Co, which emits 1173 keV and 1332 keV gammas, and recording the peak positions in ADC. Then a plot of the true energy against the mean energy peaks in ADC can be made as shown in Figure 8.4.

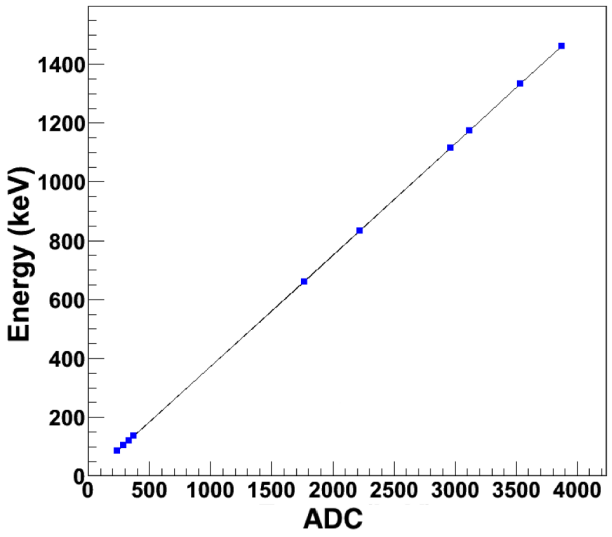

Figure 8.4: Energy calibration using ^{137}Cs, ^{60}Co, ^{57}Co and the MGS fitted to obtain the energy to ADC conversion.

8.2.2 Resolution Calibration

The width of peaks at the various energies were also measured during the energy calibration. This is necessary as the analysis of the gamma-ray spectrum is performed automatically by the analysis programme which needs to know the shape of a peak and define fits to the $\pm 3\sigma$ region. The resolution of the detector is defined as the ratio of the σ to the mean energy of the gamma peak and can be plotted as shown in Figure 8.5.

8.2.3 Efficiency Calibration

In this case efficiency refers to the detection efficiency, ε, of a particular gamma line which is defined as the ratio between the number of counts detected in a peak to

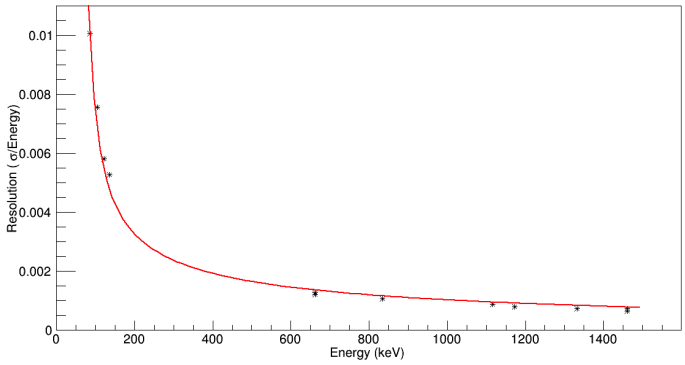

Figure 8.5: The detector energy resolution plotted here as a function of the mean energy. The red curve is fitted to guide the eye only.

the number of gamma of that energy emitted by the source. It is calculated from Monte Carlo (MC) simulations using Geant4 [65] by constructing a source with known number of gamma ray emissions and energies then analysing the resultant spectrum. For each material measurement, the MC must be tailor made as it is heavily dependent on the sample geometry and location on the detector.

The reference data for gamma ray energies, the branching ratio of each decay process and the nuclide half-life used for generating the MC were sourced from the National Nuclear Data Center [57].

To ensure the MC was reliable, a detailed description of the internal schematic of the magnesium endcap including cooling pin and their exact composition was obtained from the detector manufacturer. This was then added into the simulations.

To verify the detection efficiency MC, the activities of the MGS were calculated from the one hour calibration measurements and compared with that of the certified values. The shape, position and geometry of the MGS were measured and simulated using GEANT4 in order to verify results with simulated data. The MGS is concentrated at a point inside a plastic disk as show in Figure 8.6.

A plot of the MGS spectrum generated using MC is shown in Figure 8.7 and this is compared with the spectrum of the same source obtained for calibration. Within the associated uncertainties, the two spectrums show good agreement. This can be further improved by calibrating using a source known to a better precision.

To indicate the detector efficiency, a hypothetical point source placed 5mm above the detector was simulated and shown in Figure 8.8.

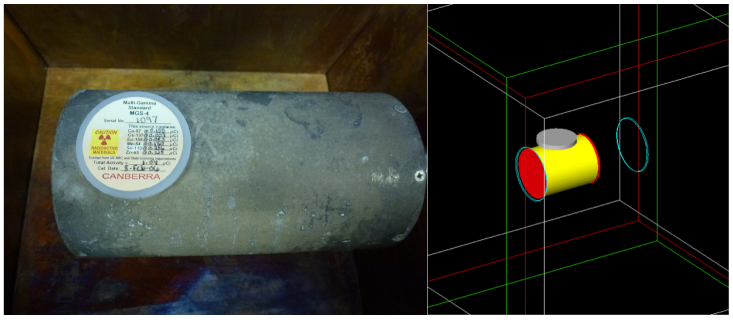

Figure 8.6: (Left) The MGS on the detector endcap for measurement. (Right) Simulated MGS on detector endcap at the same location in order to determine detection efficiency.

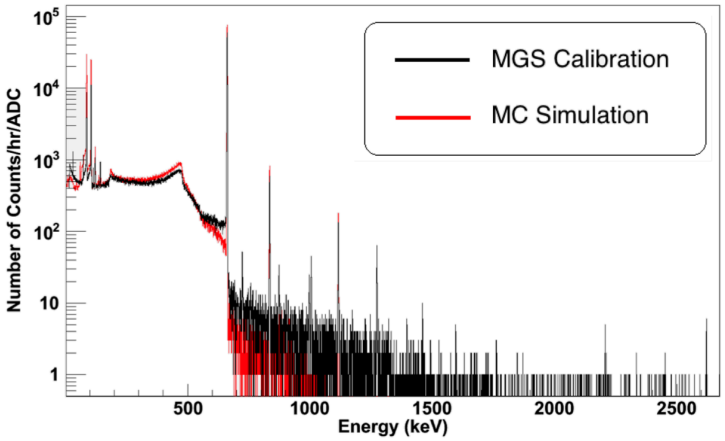

Figure 8.7: Superposition of two one hour spectrums of a MGS, with the data shown in black and MC in red.

8.3 Analysis method

For the purpose of measurements for SuperNEMO, there are 13 gamma energies of interest, mainly as a result of the ^{238}U/^{232}Th decay chains as summarised in Table 8.1. They can be used to determine the level of ^{238}U/^{232}Th contamination inside a sample, which cannot be detected directly as they do not beta decay.

The energy spectra are saved as individual hourly files over the measurement period. This provides the ability to isolate and remove outlier files from time of high detector noise such as during nitrogen refills. The remaining files are then combined into a single file containing the full spectra for analysis.

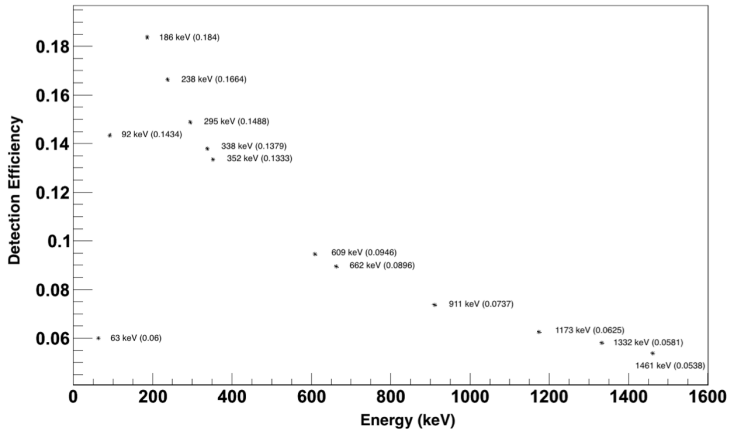

Figure 8.8: The simulated detector efficiency for a point source placed directly above the detector. The 13 points are the efficiencies at the gamma energies of interest for SuperNEMO material measurements. The efficiency at each individual point is shown inside the brackets.

Table 8.1: Energies regions of interest for use in determining U, Th and K contamination during SuperNEMO material screening

Decay Isotope	Energy (keV)	Chain/Nuclide	Branching Ratio
^{238}U	63	^{234}Th→^{234}Pa	0.037
	92	^{234}Th→^{234}Pa	0.042
	295	^{214}Pb→^{214}Bi	0.184
	352	^{214}Pb→^{214}Bi	0.356
	609	^{214}Bi→^{214}Po	0.455
^{235}U	186	^{235}U→^{231}Th	0.572
^{232}Th	238	^{212}Pb→^{212}Bi	0.436
	338	^{228}Ac→^{228}Th	0.113
	911	^{228}Ac→^{228}Th	0.258
^{137}Cs	662	^{137}Cs→^{137}Ba	0.851
^{60}Co	1173	^{60}Co→^{60}Ni	0.999
	1332	^{60}Co→^{60}Ni	1
^{40}K	1461	^{40}K→^{40}Ar	0.107

The spectra were analysed using ROOT [66] and the gamma peaks for each of the 13 energies were fitted. The integrated counts in the $\pm 3\sigma$ energy region were calculated,

then using ROOT, the background continuum was fitted and subtracted from the peak areas as shown in Figure 8.9.

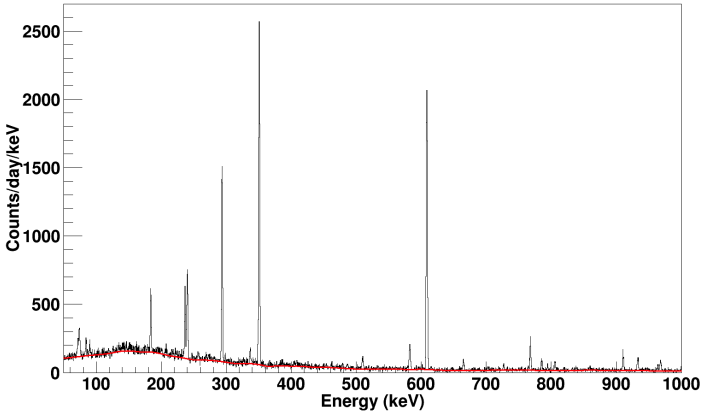

Figure 8.9: A PMT spectrum is shown to demonstrate the background continuum subtraction applied using ROOT. The spectrum is shown in black and the modelled background continuum in red.

From MC the detector efficiency at each of the energies can be determined allowing the actual number of gammas emitted at each energy to be calculated. Then, taking into account the branching ratio the sample's activity can be determined, usually expressed as Bq/kg. The equation is as follows;

$$A = \frac{N}{\varepsilon \cdot B \cdot M \cdot t} \tag{8.2}$$

where A is the sample specific activity measured as Bq/kg, N is the background subtracted number of counts, ε is the detection efficiency, M the sample mass and t the total measurement time in seconds.

The sample activity can be converted to concentrations of radioactive nuclides using the isotope mass (g/mol) and the isotope half-life. The conversion factors used were based on those calculated and published by the UK Dark Matter Collaboration [67].

For ^{238}U the gamma-lines from the decay of ^{214}Pb and ^{214}Bi were used assuming equilibrium between the parent and daughter isotope levels. For ^{232}Th the gamma-lines from ^{228}Ac, ^{212}Bi and ^{208}Tl were used.

8.3.1 Leading Industry Analysis Method

Canberra has developed a software called Laboratory SOurceless Calibration Software (LabSOCS) in order to determine sample activity and contamination. It uses a MC based analysis which includes a list of fully characterised Canberra detectors which can be selected and incorporated into simulations of detection efficiency. The characterisation procedure involves determining the detector response to a point source being placed within a 500 m radius, centred around the detector in free space, over an energy range from 10 keV to 7 MeV [68]. The software allows for selection of sample geometry based on commercially available containers as well as providing the ability to enter details of bespoke geometry designs made of materials which can be selected from a pre-defined library or constructed by user based on chemical composition.

For each sample measurement the software requires; the sample geometry, composition and its location in the detector to produce an efficiency curve. The software is able then to take a measured spectrum, fit the energy peaks and subtract the background spectrum. Then taking into account the efficiency curve it is able to produce a value for the activity of the various peaks and convert this into a measurement of the radioactive contamination.

The LabSOCS software is integrated in the Genie 2000 gamma-ray spectrometry system used for spectrum capture of Canberra HPGe detectors. This allows the entire process of data capture, detector calibration, efficiency calculation and spectrum analysis to be completed using one software.

This in essence combines the various analysis steps and programmes described in the previous section of this chapter. However, LabSOCS use is limited to characterised detectors only. Even for those characterised detectors the efficiency calculation is simulated in free space with the sample and detector only and no description of the detector shielding. Therefore, it does not take into consideration any gamma-ray interaction with materials surrounding the detector and the sample, which can result in missing backgrounds, such as backscattering and Compton scattering.

The efficiency calibration curve generated by LabSOCS also requires the user to enter the associated uncertainties. The manufacturer recommended uncertainties for standard laboratory conditions ranges from 7% at low energies (50-100 keV), 6% at medium energies (100-400 keV) and 4% at high energies (400-7000 keV). These values are significantly higher than what is achievable with standard source based calibrations, hence it cannot yet be used for very high quality measurements.

8.3.2 Automated Analysis

Motivated by the near autonomous LabSOCS the analysis steps and codes described in the first section of this chapter were integrated into one single analysis code, detailed here. Firstly all data files are selected and the noise files removed. Then a energy and resolution calibration is run based on the peaks in the data. The detection efficiency must be determined separately for each measured sample using a separate GEANT4 simulation.

Next, a file analysis script is called to sum the individual files, plot the energy spectrum and fit the predetermined energy peaks. The background continuum and peaks in the $\pm 3\sigma$ region are subtracted from the measured spectrum. The code then takes the efficiency determined by MC and the branching ratio to give the activity in Bq/kg which is then converted to a uranium, thorium and potassium contamination for each sample. The fitted plots are then written out as a PDF file, with each analysed peak saved in the format shown in Figure 8.10.

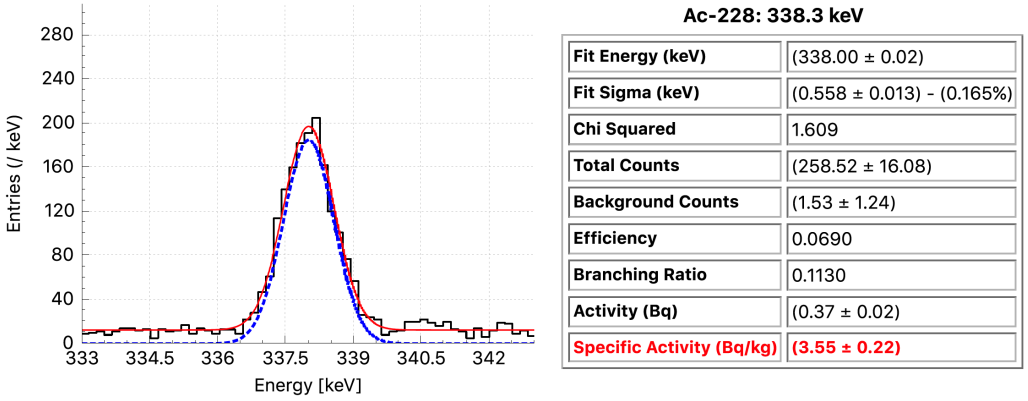

Figure 8.10: The ^{214}Pb decay peak at 295 keV. The red and blue curves shows the peak fit before and after subtraction of the background continuum respectively.

This analysis resembles the LabSOCS system, the crucial difference being efficiency determination performed using GEANT4, taking into account the shielding effects around the detector and source, producing a more accurate estimate of detection efficiency. This analysis has been used for all four current Boulby detectors and has demonstrated excellent agreement in measurements of cross calibration sources.

8.4 Background Measurements

Stable and repeatable low background activities are essential to achieving the best minimum detectable activity (MDA) possible for a HPGe detector. The background activity of each detector was periodically measure to monitor for stability and active measures were taken to modify the detector to achieve the best possible detector MDA. After each modification to the detector and shielding, the background was remeasured to determine if any changes had occurred.

8.4.1 Radon Effects and Measurements

A main source of unstable backgrounds in gamma-ray spectroscopy is the presence of radon isotopes in the air which varies depending conditions such as temperature, pressure and time of the day. The radon isotopes in the air results from emanation of trace amounts of ^{238}U and ^{232}Th producing ^{222}Rn (radon) and ^{220}Rn (thoron) respectively. Although individually neither have significant gamma-ray emissions, their decay daughters do, as summarised in Table 8.2;

Table 8.2: The daughter nuclides of radon isotopes which emit gamma-rays and their respective energies.

Radon Isotope	Chain/Nuclide	Energy (keV)
^{222}Rn	^{214}Pb→^{214}Bi	295
	^{214}Pb→^{214}Bi	352
	^{214}Bi→^{214}Po	609
^{220}Rn	^{212}Pb→^{212}Bi	238

There are three steps which can be taken to reduce the effects of radon isotopes inside the detector volume;

- make the detector shielding as air-tight as possible to prevent radon diffusion into the detector volume;
- reduce the volume of air inside the detector volume by filling it with sealed containers filled with radon-free air such as nitrogen or helium;
- flushing the central detector volume with radon free gas such as nitrogen to actively remove the radon isotopes whilst creating an overpressure to suppress radon diffusion.

All three options would require, to some degree, a reduction in accessibility to the detector. Given the relatively long half-life of ^{222}Rn and its high diffusibility, it would be difficult to construct a seal sufficiently air tight to prevent diffusion. In particular, there is a path in the current shielding configuration for the stem of the detector to pass through into the central volume. Even if this were possible, there would still be significant contribution of radon as a result of emanation from the Pb and Cu. Even ^{220}Rn which has a relatively short half-life of just 55 seconds, can still diffuse through the outer shielding into the central volume before decaying into daughter isotopes.

Placing sealed containers to displace the air inside the detector has been shown to result in significant reduction in radon contributions to background measurements. However, this requires the containers to have very low radon emanation themselves as well as developing a method fill and seal them to a satisfactory quality.

Continuous flushing offers the most practical solution to reducing radon isotopes inside the central volume. All four detector castles were designed to be as air tight as possible and to accommodate an active purging line to flush the detection volume using either cylindered or boil off nitrogen.

8.4.2 DURRIDGE RAD7 Study and Measurements

The RAD7 made by 'Durridge Radon Instrumentation' is a portable, fast and highly sensitive radon detector. It consists of a 0.7 litre spherical detection volume which has an electrical conductor coated on the inside surface. The centre of the volume consists of a solid-state, ion-implanted, planar, silicon alpha detector [69].

The RAD7 detector does not measure 222Rn directly, instead it measures the daughter isotopes ^{218}Po, ^{214}Po and ^{210}Po. The ^{218}Po, which is positively charged, is plated onto the detector as a result of the electric field. It also detects the ^{220}Rn daughter isotopes ^{216}Po and ^{212}Po for thoron measurements. The data is recorded and can be analysed using the software CAPTURE [70]. Other than the number of polonium counts detected, the RAD7 device also records the temperature and humidity of the air it measures.

A separate analysis code was written in order to analyse the RAD7 data using ROOT independently of CAPTURE. This is in part due to the lack of clarity as to the statistical methods applied by the CAPTURE software in processing the data. This required an extensive study of the RAD7 detection efficiency to the radon decay daughters as well as the humidity correction factor.

RAD7 Intrinsic Background

The RAD7 was placed inside a sealed air tight stainless steal container which was flushed using cylindered nitrogen, at a rate of 5 l/min, in order to determine its absolute sensitivity. A fan was installed on the inside of container to ensure uniform distribution of nitrogen.

Measurement was made over an 18 hour period and the resultant radon levels are shown in Figure 8.11. The detected radon level demonstrates an intrinsic background of 0.1 Bq/m^3 for the RAD7 detector.

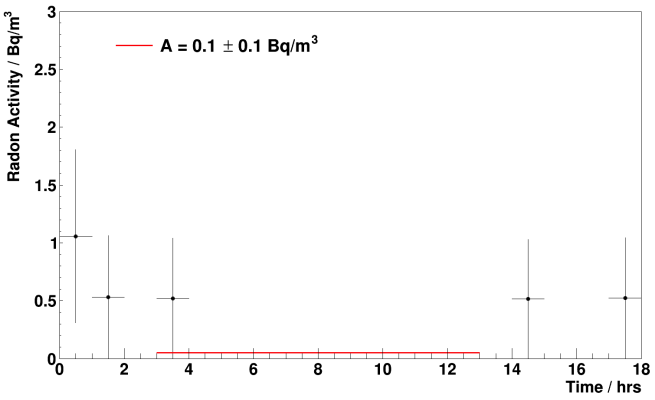

Figure 8.11: RAD7 background measurement, operating without the desiccant column, over 18 hours.

Radon Level Measurements

Having measured the intrinsic background of the RAD7 and tested the analysis code. The detector was brought underground to monitor and measure the radon levels inside the underground laboratory, in particular the areas around the germanium detector.

The RAD7 was setup with a desiccant drying column to remove the input humidity, and placed on a table top next to the HPGe detector. A 2 day background measurement was taken and the result is shown in Figure 8.12. There appears to be a spike in radon levels in the morning from 6 am to 11 am with unknown origin. However, analysing the data before and after the spike separately, the results are relatively consistent and agree with each other within uncertainties.

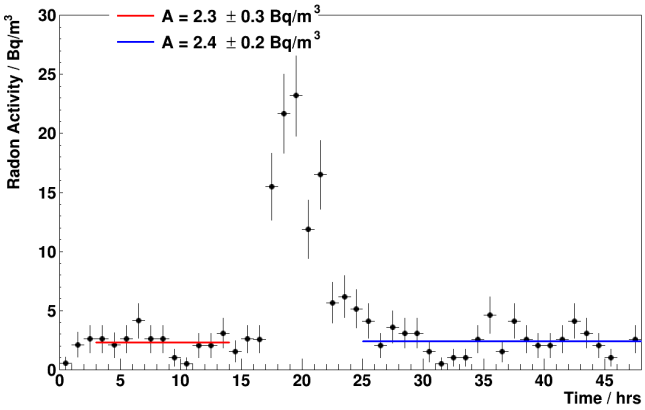

Figure 8.12: RAD7 measurement with the standard setup up over 2 days.

Following this measurement, a second measurement was made over a 10 day period giving much greater statistics. The resultant plot is shown in Figure 8.13, and the radon levels appear to be much more stable for the duration of measurement.

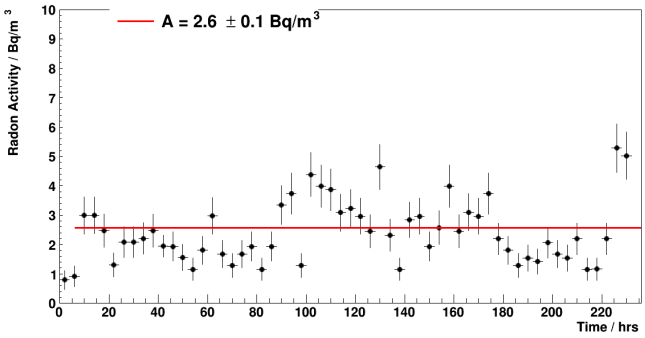

Figure 8.13: RAD7 measurement with the standard setup up over 10 days.

Combining the three data sets, taking into account the associated uncertainties, gives a radon level of 2.5±0.1 Bq/m^3 inside the laboratory.

8.4.3 Nitrogen Flushing

The customised shielding allows nitrogen to be directly flushed into the central detection volume. Cylindered nitrogen was used as the flushing gas as it has extremely low levels of radon. Since the castle is built to millimetre precision an

additional anti-radon tent was not required. The detection volume is purged at a rate of 1 lpm and the excess nitrogen is allowed to leak out, creating an active flow suppressing radon diffusion. This gives much better accessibility to the detector for sample insertion and extraction.

The effectiveness of the nitrogen flushing system was tested by comparing the background spectrum to before and after purging and comparing the gamma lines which are as a result of radon decays.

Nitrogen flushing at 1 lpm

Firstly, a background measurement was taken over 2 weeks with the nitrogen flushing set at 1 lpm. This rate was chosen as it is used by the LSM germanium facility for radon purging. A comparison of the resultant spectrum with the pre-flushing background spectrum is shown in Figure 8.14. This shows a reduction in the radon daughter decay peaks by a factor of 4, Table 8.3.

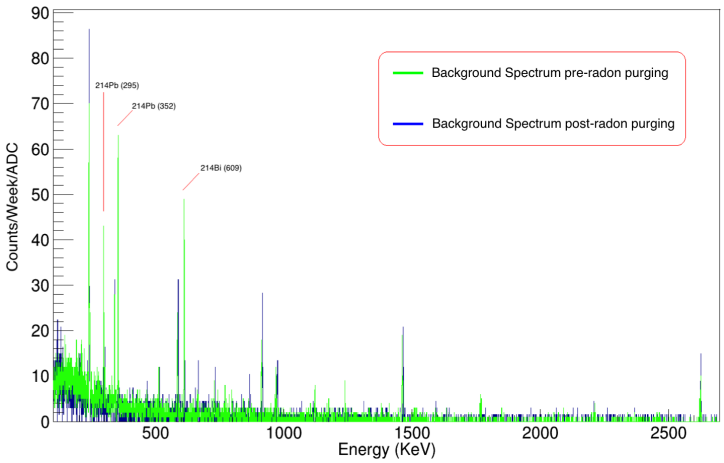

Figure 8.14: Two superimposed background spectrums taken before and after radon purging shown in green and blue respectively. The three labelled peaks are as a result of radon decay isotopes.

The integrated rate between 100-2700 keV was measured to be 0.751±0.001, a reduction on the pre-radon purging rate by more than 30%. The results also show a slight reduction in the 238 keV energy peak, more than that expected from purging purely radon. This could be as a result of thoron reduction inside the main detector volume, which could explain why only the 238 keV peak was reduced and not the 338 and 911 keV peaks.

Chain/Nuclide	Energy (keV)	Boulby HPGe ($\pm3\sigma$)	Simulated ^{222}Rn (2.5 Bq/m^3 $\pm3\sigma$)	Boulby HPGe with radon purging ($\pm3\sigma$)
^{234}Th→^{234}Pa	63	16.7±1.6	3.85±0.11	10.3±0.9
^{234}Th→^{234}Pa	92	18.8±1.7	4.41±0.12	13.9±1.1
^{214}Pb→^{214}Bi	295	31.3±2.2	27.50±0.29	9.0±0.9
^{214}Pb→^{214}Bi	352	39.9±2.5	46.00±0.38	9.8±0.9
^{214}Bi→^{214}Po	609	34.4±2.3	38.54±0.35	8.2±0.8
^{235}U→^{231}Th	186	21.3±1.8	7.60±0.15	14.4±1.1
^{212}Pb→^{212}Bi	238	84.9±3.7	5.32±0.13	71.3±2.4
^{228}Ac→^{228}Th	338	22.7±1.9	2.24±0.08	22.2±1.4
^{228}Ac→^{228}Th	911	21.8±1.9	0.72±0.05	18.8±1.3
^{137}Cs→^{137}Ba	662	6.8±1.0	1.02±0.06	6.6±0.7
^{60}Co→^{60}Ni	1173	0.5±0.3	0.39±0.04	1.7±0.4
^{60}Co→^{60}Ni	1332	1.7±0.5	0.30±0.03	1.4±0.3
^{40}K→^{40}Ar	1461	17.2±1.6	0.30±0.3	15.1±1.1

Table 8.3: Comparison of results taken before and after nitrogen flushing at 1 lpm. The areas in grey are the radon daughter isotope decays.

Nitrogen flushing at 5 lpm

The flow rate was then increased to 5 lpm in order to test if further reduction could be achieved. A new flow meter, by Key Instruments, was installed to monitor the flow rate. The results after a one week measurement are shown in Table 8.4.

The results show a slight improvement from the 1 lpm flushing results. However, there also appears to be an increase in the previously reduced ^{212}Pb peak. Given the ^{228}Ac peak has not increased this could suggest contaminates were introduced into the detector volume which emanates thoron. Given these results, a nominal flushing rate of 1 lpm was established for all Boulby detectors as they have similar interval volume.

Improvements to Sensitivity

The reduction of radon and its daughter isotopes translates to improved sensitivity for the ^{238}U lines. This can be seen in Figure 8.15, where sensitivity is plotted as a function of time for the ^{214}Bi, 609 keV, line.

Chain/Nuclide	Energy (keV)	Boulby HPGe ($\pm 3\sigma$)	Boulby HPGe with radon purging ($\pm 3\sigma$) 2 weeks at 1 lpm	Boulby HPGe with radon purging ($\pm 3\sigma$) 1 week at 5 lpm
^{234}Th→^{234}Pa	63	16.7±1.6	10.3±0.9	12.0±1.3
^{234}Th→^{234}Pa	92	18.8±1.7	13.9±1.1	19.5±1.6
^{214}Pb→^{214}Bi	295	31.3±2.2	9.0±0.9	8.0±1.1
^{214}Pb→^{214}Bi	352	39.9±2.5	9.8±0.9	8.3±1.1
^{214}Bi→^{214}Po	609	34.4±2.3	8.2±0.8	5.5±0.9
^{235}U→^{231}Th	186	21.3±1.8	14.4±1.1	13.4±1.4
^{212}Pb→^{212}Bi	238	84.9±3.7	71.3±2.4	81.7±3.4
^{228}Ac→^{228}Th	338	22.7±1.9	22.2±1.4	16.6±1.5
^{228}Ac→^{228}Th	911	21.8±1.9	18.8±1.3	17.8±1.6
^{137}Cs→^{137}Ba	662	6.8±1.0	6.6±0.7	5.0±0.8
^{60}Co→^{60}Ni	1173	0.5±0.3	1.7±0.4	2.2±0.6
^{60}Co→^{60}Ni	1332	1.7±0.5	1.4±0.3	2.2±0.6
^{40}K→^{40}Ar	1461	17.2±1.6	15.1±1.1	15.5±1.5

Table 8.4: Comparison of results taken during nitrogen flushing at 1 lpm and 5 lpm. The areas in grey are the radon daughter isotope decays.

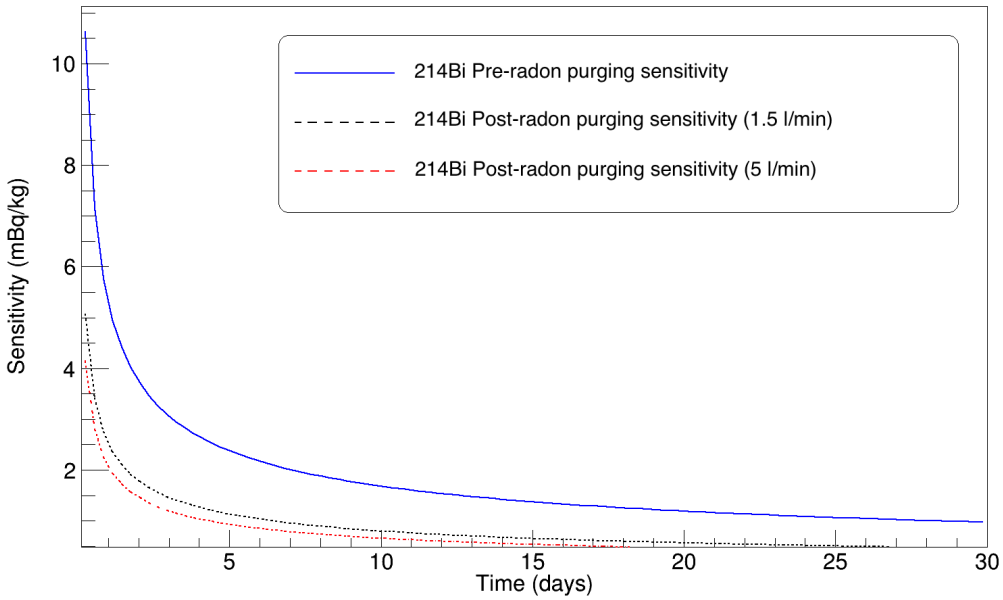

Figure 8.15: Sensitivity plot of the ^{214}Bi line for no nitrogen flushing, 1 l/min and 5 l/min shown as blue, black and red respectively.

8.4.4 Shielding improvements

The first version of shielding constructed was using interlocking lead bricks, 100 mm, followed by plates of copper, 100 mm. The lid was made from a single lead block which had to be removed using a crane. Nitrogen flushing was achieved by feeding a gas line through the gap at the neck of the detector and an anti-radon shield was built around the castle. This design was impractical due to the time required to open and close the detector per sample insertion, in particular for calibration samples.

A new castle was designed with millimetre precision with the same thickness of lead and copper. The advantage of the new castle design is complete replicability of the castle geometry, ease of access to the detector and allows for built in nitrogen purging system. Care was taken to clean both the lead and copper before assembly. A comparison of the old and new castles are shown in Figure 8.19.

After the detectors were installed into the new castle, they were calibrated and a background measurement was taken. From this the integrated counts from 100-2700 keV were determined and compared with data taken before the shielding modifications showing a factor 2 improvement. The result are shown in Table 8.5. However, when compared against world leading low background detectors such as Gator currently

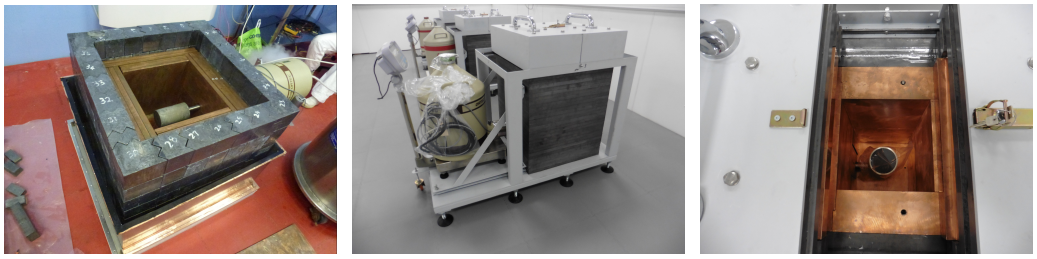

(a) Old Shielding **(b)** New Shielding **(c)** New Shielding Lid Open

Figure 8.16: Comparison of old and new shielding for Boulby germanium detectors.

being operated at Gran Sasso underground laboratory [71] there are still significant improvements to be made.

Detector Configuration	Events / min
Boulby initial state	1.303 ± 0.005
Boulby + cleaning	1.081 ± 0.003
Boulby + nitrogen flushing	0.751 ± 0.001
Boulby + shielding modification + nitrogen flushing	0.35 ± 0.004
The Gator facility (LNGS)	∼0.16

Table 8.5: Comparison of integrated counts over the range 100-2700 keV between stages of detector improvement at Boulby and the world leading ultra low background germanium detector.

The new shielding design allows all current and future detectors to interchange shielding depending on measurement requirements. This means a detector is not limited to a single detection volume and can be placed in a larger castle if required by sample dimensions.

8.5 Detector Relocation

A new underground facility was constructed at Boulby to replace the old laboratory building. The building of the new facility gave the opportunity to construct a dedicated low background measurement space called the Boulby Underground Germanium Suite (BUGS). BUGS is designed as a class 1000 cleanroom with; air conditioning to maintain stable temperature, nitrogen gas line to deliver purging gas

for HPGe detectors and a sample preparation area. The cleanroom further minimises background variation as it reduces the level of contaminates in the air. All four detectors have been relocated inside the new facility and have been fully operational since April 2016.

8.6 Minimum Detectable Activity

The MDA is the minimum amount of radioactive nuclide which can be confidently detected given the parameters of a specific measured spectrum. The method used to find the MDA of a germanium detector is the same as was outlined in Section 6.2.

The MDA, A_D, can then be found using:

$$A_D = \frac{N_D}{Br \cdot \varepsilon \cdot t} \tag{8.3}$$

where Br is the branching ratio of decay, ε is the the detection efficiency and t is the measurement time. Using this relationship the MDA of each HPGe detector to ^{238}U and ^{232}Th as a function of time was calculated using the ^{214}Bi and ^{212}Pb lines respectively, the results are shown in Figure 8.17. The detection efficiency used to estimate the sensitivity was taken from a GEANT4 simulation result of a 100 g IAEA-385 calibration source placed directly at the centre of the detector end cap.

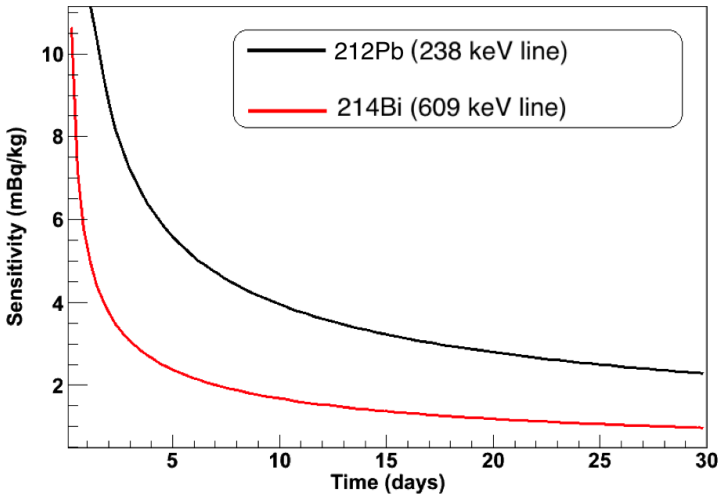

Figure 8.17: Sensitivity plotted for ^{238}U and ^{232}Th using the ^{214}Bi and ^{212}Pb lines respectively

8.7 Optimising source geometry

The achievable sensitivity depends on the inherent background in the detection volume and the detection efficiency of the measured sample, related by the equation [72];

$$A = \sqrt{b + tB + t^2\sigma_B^2} \cdot \frac{1}{(\varepsilon M t)} \tag{8.4}$$

Where A is the activity (Bq/kg), b is the background continuum, t is the measurement time, B is the background counts, σ_B error on the background, ε is the detection efficiency and M the sample mass. The activity detected increases with mass until self-absorption of the sample dominates. The detection efficiency of a source can be maximised using MC simulation to determine the optimum sample geometry. Hence, each sample can be optimised for measurement.

8.8 Material Screening

Prior to preparing a sample for screening it is important to determine which detector is best suited for taking the measurement. The key factors are; the gamma lines of interest, sample mass and geometry. An example of a standard germanium measurement is presented below.

8.8.1 Sample Preparation

The sample measured was the external screws used to construct the SuperNEMO Demonstrator module. The sample was first ultrasonically cleaned using Leksol, an industrial degreasing solvent. Then a total of 6.09 kg of the screws sample was inserted into a 1.46 litre marinelli and sealed for measurement, as shown in Figure 8.18. This was carried out inside a cleanroom environment. Once the sample was prepared, it was wrapped and taken underground for measurement.

8.8.2 Simulation and Measurement

Once inside BUGS, the sample was unwrapped and the outside of the marinelli was wiped down using IPA to remove any contaminants. The sample was then placed directly on top of the detector end cap for measurement, as shown in Figure 8.19a. This configuration was then be simulated using GEANT4, as shown in Figure 8.19b, to extract a detection efficiency, as shown in Figure 8.20.

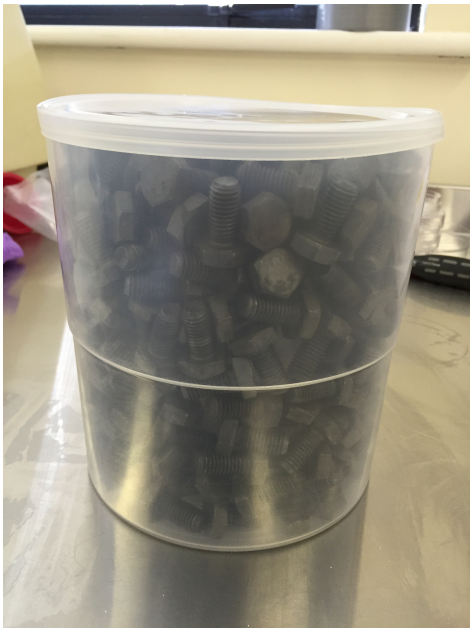

Figure 8.18: SuperNEMO external screws contained with marinelli for measurement.

Using the detection efficiency and the known detector background, it is possible to calculate the duration of measurement necessary to screen a sample below a desired level of sensitivity.

8.8.3 Analysis and Results

After a 10 day measurement, the resultant spectrum was analysed and the net count of individual gamma peaks in the $\pm 3\sigma$ region of interest were fitted. The specific activity of each gamma line was then be calculated using (8.2) and the main results are summarised in Table 8.6.

These results are excellent and well below the requirement level for Demonstrator construction.

(a) Sample on HPGe detector for measurement.

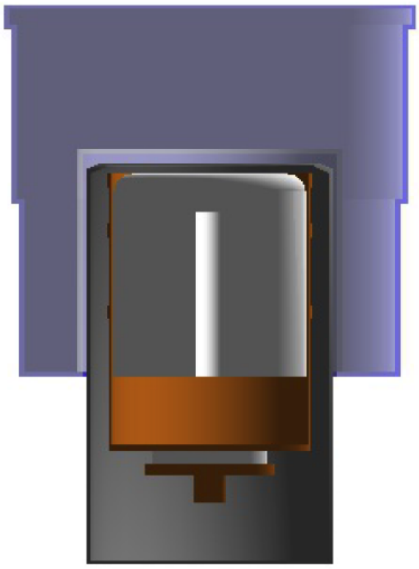

(b) Simulation of sample on HPGe detector.

Figure 8.19: Sample of SuperNEMO external screws during HPGe measurement and the simulated sample geometry.

Table 8.6: The daughter nuclides of radon isotopes which emit gamma-rays and their respective energies.

Isotope	Specific Activity (mBq/kg)
^{238}U (Early)	18.66 ± 3.94
^{214}Bi	3.09 ± 0.37
^{232}Th (Early)	1.71 ± 0.45
^{208}Tl	0.86 ± 0.38
^{40}K	13.04 ± 3.63

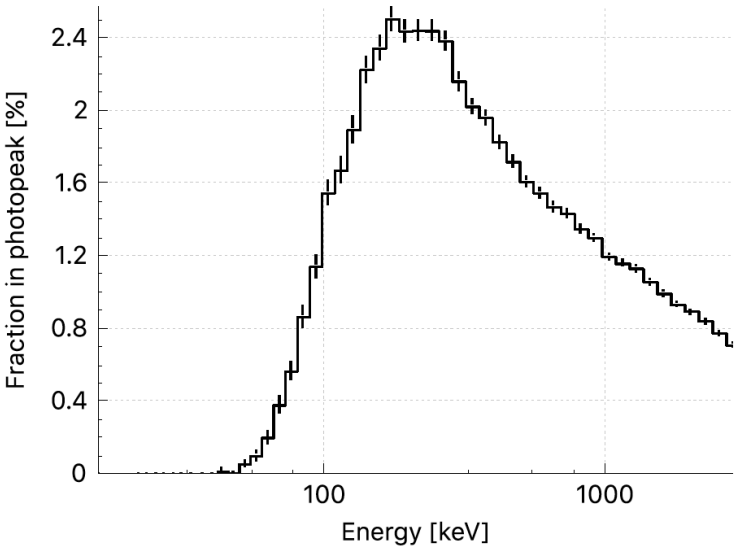

Figure 8.20: Simulated detection efficiency of the SuperNEMO external screw sample as a function of energy.

Chapter 9

Measurement of ^{96}Zr Decay to Second Excited State

"One day I will find the right words, and they will be simple."
- Jack Kerouac

The problems associated with precise calculations of NME were described in Section 2.9. If the $0\nu\beta\beta$ decay was observed the uncertainty associated with the NME would place the largest uncertainty on the determined effective neutrino mass. Results of $2\nu\beta\beta$ decay half-lives from experiments such as NEMO-3 provide additional information to validate and modify NME calculation parameters. The measurement of decay modes to excited states can shed more light on the nuclear structure of the decay and may be able to be used as a consistency check for single isotope $0\nu\beta\beta$ experiment to discriminate between true signal and unknown background.

There are 11 isotopes which have been observed to undergo $2\nu\beta\beta$, however, there has only been two (^{100}Mo and ^{150}Nd) which have been observed to undergo a $2\nu\beta\beta$ decay to the first excited 0^+ state. A good candidate for a third observation of decay to the first excited state would be ^{96}Zr in light of its high phase space and Q value.

9.1 Double Beta Decay of ^{96}Zr

The decay of ^{96}Zr to excited states is followed by a decay to the ground state via γ-ray emissions. These gammas can then be detected using a HPGe detector such as the detector described in Section 8.1.1. The Q values of the ground and first excited state are;

$$Q_{\beta\beta}(0_0^+) = 3.35MeV, \qquad Q_{\beta\beta}(0_1^+) = 2.20MeV \tag{9.1}$$

Therefore, the phase space of the decay to the first excited state is greatly reduced as a result of the lower Q value. The decay of ^{96}Zr to ground state as measured by

the NEMO-3 collaboration;

$$T_{1/2} = 2.35 \pm 0.14(stat) \pm 0.16(syst) \times 10^{19} \text{ yr} \tag{9.2}$$

There was no observation of decay to the excited states, however, from the half-life of the decay to ground state it is possible to to predict the expected decay half-life to the first excited state to be $T_{1/2} > 2.1 \times 10^{21}$ yr [73]. However, a more recent publication on a systematic law for half-lives of β-decay estimates the decay of ^{96}Zr, to the first excited 0^+ state, to have a half-life of $2.59{\times}10^20$ yr [74]. This prediction has been excluded at 93% C.L. by the current world best limit on decay of ^{96}Zr to the first excited state of Mo96 at $T_{1/2} > 3.1 \times 10^{20}$ yr (90% C.L.) [75].

The large Q value of the decay of ^{96}Zr means that several excited states of ^{96}Mo could exist, as shown in Figure 9.3. The main decay mode of interest are gammas emitted from the de-excitation of ^{96}Mo from the first excited state, $0_1^+ \rightarrow 2^+ \rightarrow 0^+$, which will produce two gammas at 369.8 and 778.2 keV respectively.

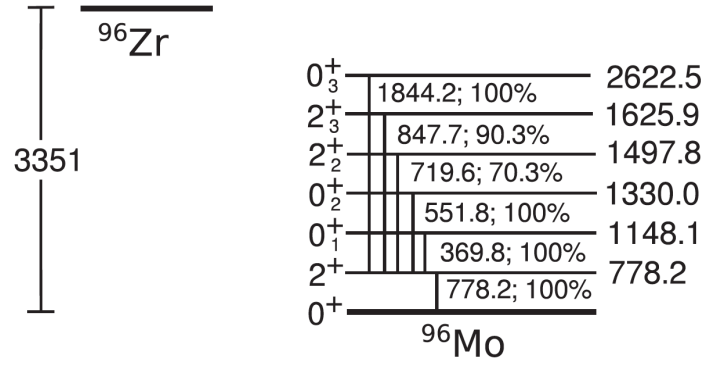

Figure 9.1: The decay states for ^{96}Zr to ^{96}Mo.

An experiment can be design to measure a large sample of ^{96}Zr to detectd these de-excitation gammas, thus measure the half-life of the decay to the first excited.

9.2 Experimental Method

9.2.1 The Detector

The experiment will consist of a single ultra-low background Canberra Lingolsheim coaxial detector with a crystal volume of 600 cm^3. This detector will be surrounded on all sides by a custom made castle consisting of 1 cm of ultra radio-pure OFHC

copper followed by 9 cm of high purity copper and then 10 cm of low radio-activity lead. The central volume will be purged continuously with nitrogen to suppress radon levels. The entire experimental setup would ideally be located underground, for example at the Boulby Underground Laboratory.

9.2.2 The sample

In order to improve on the current world limit a substantial mass of isotope is required for measurement. In it's natural form zirconium only contains 2.8% of the isotope ^{96}Zr, so to increase isotope mass, the sample must either be enriched or increased in mass. Enrichment can increase isotope abundance to above 90%, this also has the added bonus of increasing the radio-purity of the sample as the enrichment process also eliminates most of the nuclear contaminants. Enrichment can only be done using electromagnetic separation (EMS) which is incredibly expensive and also has a low production rate. The simplest way to gain extra ^{96}Zr mass is by increasing the mass of zirconium measured which is also relatively cheap. However, it is essential to select a sample which is as radio-pure as possible, otherwise the sensitivity will be severely limited by background.

For this measurement several samples of ultra-pure zirconium oxide (ZrO_2) samples, 100 grams each, were purchased from various suppliers to be screened for radio-purity. Zirconium oxide was used instead of pure zirconium as the sample was needed in its powdered form for preparation into containers and pure zirconium in powdered form is highly flammable and may spontaneously ignite in air.

A special container, as shown in Figure 9.2a, was selected, due to its radio-purity, to house the sample for HPGe measurements. The container was cleaned using an ultrasonic bath filled with IPA then left to dry in a class 10,000 cleanroom. The samples were delivered in nitrogen sealed bottles which were only opened once inside the cleanroom. The samples were packaged inside the container which was weighed before and afterwards, as shown in Figure 9.2.

9.2.3 Zirconium Oxide Selection Result

A screening programme was carried out to screen five separate samples of ZrO_2 using the Boulby well detector. The results showed a high level of U and Th contamination for all the samples, as shown in Table **??**.

Although these observed activities are higher than ideal it is not entirely unexpected due to contamination of natural zirconium oxides. There exists processes of physical and chemical purification which can remove the U and Th content, for further detail please see [76]. These techniques have been developed through 15 years of R&D for

(a) Sample containers

(b) Samples

(c) Empty container

(d) Full Container

Figure 9.2: Sample preparation procedure for HPGe measurement.

Chain/Nuclide	Energy (keV)	Boulby HPGe ($\pm3\sigma$)	Boulby HPGe with radon purging ($\pm3\sigma$) 2 weeks at 1 lpm	Boulby HPGe with radon purging ($\pm3\sigma$) 1 week at 5 lpm
^{234}Th→^{234}Pa	63	16.7±1.6	10.3±0.9	12.0±1.3
^{234}Th→^{234}Pa	92	18.8±1.7	13.9±1.1	19.5±1.6
^{214}Pb→^{214}Bi	295	31.3±2.2	9.0±0.9	8.0±1.1
^{214}Pb→^{214}Bi	352	39.9±2.5	9.8±0.9	8.3±1.1
^{214}Bi→^{214}Po	609	34.4±2.3	8.2±0.8	5.5±0.9

Table 9.1: Comparison of results from measurements of zirconium oxide samples.

NEMO-3 and continue as part of the preparation of the SuperNEMO source ^{82}Se. This technique has demonstrated a 2 order of magnitude reduction factor in nuclear contaminants. The process of purification still remain considerably cheaper than enrichment.

9.2.4 Sample Holder

Once a sample has been selected it will be placed inside a specially designed marinelli which has been geometrically designed to optimise detection efficiency, as shown in Section 9.3.2. The marinelli must be made from an extremely radio-pure material and have thin walls to ensure gammas are not obstructed by the container wall.

Several materials were considered but it was decided a marinelli constructed using Duracon with an internal volume of 1.8 litres holding 10-20 kg of sample would be optimal. Experiments to find a 3D printing material of sufficient radio-purity were also conducted, as well as attempting to make Duracon into printing filaments. The result does not suggest a 3D printed marinelli can replace the conventional machine produced Marinelli containers at the current time for reasons of radio-purity. Once the sample is inserted into the Marinelli, it will sit directly above the detector end cap for measurement.

9.2.5 Measurement

The sample can be placed directly over the end cap for measurement. The Boulby germanium facility maintains a constant temperature which is monitored along with the rate of nitrogen purging to ensure measurement stability. In general HPGe detectors produce very stable gamma ray spectrums over long periods of measurement, however, there can be small drifts in the gamma peaks with time. Therefore, the

detector should be calibrated on a weekly basis using a gamma source with known activities to ensure valid measurement results.

9.3 Sensitivity Study Results

MC studies were conducted using GEANT4 simulations to determine the potential half-life sensitivity of an experiment using up to 30 kg of highly pure natural zirconium oxide and a large HPGe detector for one to two years of counting. The predicted experimental sensitivity was determined using the formula;

$$T_{\frac{1}{2}} > ln(2)\frac{t \cdot Br \cdot N_0 \cdot \epsilon_D}{D_L} \tag{9.3}$$

where t is the exposure time, Br is the branching ratio, N_0 is the number of nuclei, ϵ_D is the detection efficiency and D_L is the detection limit. The definition of detection limit as stated in Section 6.2 was used. In this study, B is taken as the background counts in the $\pm 3\sigma$ region around the gamma energies of interest.

9.3.1 Background Estimates

Simulations were carried out to determine the background contribution of a zirconium sample if it were purified using the method proposed in Section 9.2.3, with a factor 100 reduction in all contaminates. From the resulting spectrum the background contribution of the sample to the energy regions of interest can be determined. This sample background is then added to the inherent detector background results of which are taken from an existing ultra low background Lingolsheim HPGe detector upon which the simulated detector geometry is based. The detector only backgrounds are 1.20±0.19 and 0.53±0.12 cpd in the $\pm 3\sigma$ region of gamma energies 369 and 778 keV respectively.

9.3.2 Detection Efficiency Monte Carlo

The simulated detection efficiencies were found using geometry based on the aforementioned ultra low background detector. The accuracy of the GEANT4 simulations were tested by comparing the simulated detection efficiency results of a calibration source to an actual measurement of the source with known gamma activities, the results were in close agreement.

After the simulated detector results had been verified simulations were carried out to determine the optimum geometry of a marinelli beaker in order to maximise detection efficiency. In theory this should be a container which evenly distributes

the zirconium oxide sample on all sides to increase angular coverage and minimise sample self shielding and this was found to be true, as shown in Figure 9.3. Due to

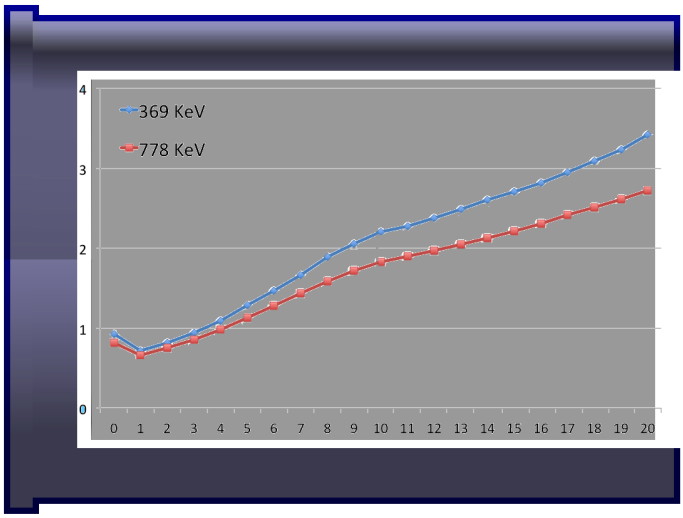

Figure 9.3: The detection efficiency at 369 and 778 KeV for 10 kg of ^{96}Zr as varying marinelli geometry.

geometrical constraints placed by the cold finger, the marinelli cannot extend over the side of the end cap by more than 13 mm. Therefore, a marinelli which extends 10 mm past the bottom of the end cap is chosen as the optimum sample geometry for maximal detection efficiency.

9.3.3 Experimental Potential

Using the optimised geometry discussed above the detection efficiency for a range of sample masses were simulated and the potential sensitivities that can be achieved were estimated, as shown in Table 9.2. The sensitivity estimates is based on a purified zirconium oxide sample contained within a radio-pure marinelli placed on a detector with the same background as found in prior measurements as stated above.

The study shows even with a modest 10 kg of radio-pure natural zirconium oxide and one year of measurement the experimental setup can produce a factor 2 improvement on the existing best limit.

The background levels of the HPGe detector can be further improved by replacing the end cap and internal components with the latest materials of greater radio-purity

Mass	Detection Efficiency		1 Year Half-life (yr)		2 Year Half-life (yr)	
(kg)	369.8 keV	778.2 keV	369.8 keV	778.2 keV	369.8 keV	778.2 keV
10	3.397	2.69	5.97×10^{20}	7.04×10^{20}	8.52×10^{20}	1.01×10^{21}
12.5	2.967	2.396	6.52×10^{20}	7.84×10^{20}	9.30×10^{20}	1.12×10^{21}
15	2.593	2.154	6.84×10^{20}	8.46×10^{20}	9.75×10^{20}	1.21×10^{21}
17.5	2.305	1.957	7.09×10^{20}	8.97×10^{20}	1.01×10^{21}	1.28×10^{21}
20	2.087	1.791	7.34×10^{20}	9.38×10^{20}	1.05×10^{21}	1.34×10^{21}
22.5	1.89	1.621	7.48×10^{20}	9.55×10^{20}	1.07×10^{21}	1.37×10^{21}
25	1.723	1.499	7.58×10^{20}	9.81×10^{20}	1.08×10^{21}	1.40×10^{21}
27.5	1.571	1.398	7.60×10^{20}	1.01×10^{21}	1.08×10^{21}	1.44×10^{21}
30	1.462	1.307	7.71×10^{20}	1.03×10^{21}	1.10×10^{21}	1.47×10^{21}

Table 9.2: Results from simulation of ^{96}Zr sample showing detection efficiency at two gamma energies of interest and the corresponding sensitivity which can be achieved with 1 or 2 years of continuous measurement.

offered by Canberra. Better shielding and veto systems can be introduced to further suppress background levels.

Chapter 10

Conclusion

"All we have to decide is what to do with the time that is given us."
- Gandalf the Grey

Neutrino oscillations have provided the first tantalising evidence of physics beyond the Standard Model. Neutrinos are the most abundant massive particle in the universe, yet they remain one of the most illusive. The search for the $0\nu\beta\beta$ decay process has unrivalled potential to unravel many neutrino secrets such as; the absolute neutrino mass, mass hierarchy, CP-violation and its fundamental nature as well as whether the neutrino is a Dirac or Majorana particle.

This search has resulted in a vast array of innovative detector designs to look for one of nature's rarest displays. The $2\nu\beta\beta$ decay process has been, to date, the rarest nuclear decay ever observed, with half-lives in the region of 10^{18} years. Due to the complexity of NME calculations, enrichment and phase space calculations (as a factor of $Q_{\beta\beta}$ and Z mass), there is no single golden isotope. The same can be said of the detector technology with considerations for radio-purity, energy resolution, scalability and topology reconstruction, there is no single superior design which can vastly out perform the others.

The main challenge facing all future generations of $0\nu\beta\beta$ decay experiments is radio-purity. The current generation of experiments are already pushing the limits of what can be measured using existing HPGe capacity. There is not only a limitation on the sensitivity achievable with conventional HPGe detectors, but a limitation on the throughput for the few detectors capable of reaching the already demanding contamination targets. New detectors and germanium facilities must be established in order to meet the stringent demands of radio-purity. However, this alone will not be enough. New techniques of combining measurements of nuclear contamination using a range of complimentary techniques such as alpha spectroscopy and mass spectroscopy, which are optimised for specific isotopes, can significantly improve accuracy of U and Th contamination estimates from early to late in the decay chain.

The development of a large low background electrostatic radon detector coupled with emanation chambers and the RnCL, which is relatively cheap and mobile, has

major applications not only in $0\nu\beta\beta$ decay experiments but all rare event search experiments. Radon is a highly diffusive radioactive gas with a relatively long half-life. Since it is part of the U and Th decay chain, it can be found to emanate from all materials. Due to the large decay energy of the radon decay daughters, radon forms a major background to all rare event search experiments. Results from the radon detector showed a background count of ∼5 cpd which translates to a sensitivity of 0.1 mBq or 1.4 mBq/m^3 (90% C.L.).

Two emanation chambers have been constructed to be used in conjunction with the radon detector to carry out radon emanation measurements optimised for small samples with a large surface area. Both chamber have demonstrated excellent stable backgrounds giving them sensitivities of;

$$Chamber1 :, \qquad Chamber2 : \tag{10.1}$$

Direct measurement of radon emanation of detector components in their final configuration are critical as radon emanation is heavily geometry dependent thus this is the only way to determine the true emanation level. Both chambers have a 100% occupancy with a sample measurement rate of ∼1 sample per month.

The RnCL was calibrated post modification which has showing a factor 2 improvement in the trapping and transfer efficiency. This improvement translated to a measured sensitivity of 40 µBq/m^3 for 8.4 m^3 of gas, the volume used for a standard tracker radon measurement.

Using the RnCL a gas purification system was commissioned and tested to show a factor 20 suppression of radon activity when nitrogen is used as the carrier gas. The suppression factor is expected to be much higher, of order 10^6, for helium as the atomic size of helium is much smaller.

The RnCL was built for the measurement of radon emanation from the SuperNEMO quarter tracker modules during construction. The quarter trackers can be tested for radon emanation before and after cell insertion to disentangle the source of radon emanation. The radon measurement result from the first three of four C-Sections are as follows:

$$\begin{aligned} C0 \qquad & A > 11.37 \pm 1.44 mBq \text{ (90\% CL)} \\ C1 \qquad & A > 15.26^{+2.50}_{-3.82} mBq \text{ (90\% CL)} \\ C2 \qquad & A > 4.36 \pm 1.31 mBq \text{ (90\% CL)} \end{aligned}$$

Taking a conservative estimate of the radon activity of C3, as the average radon levels of C0-2, gives 10.33 mBq. Combining the radon activity results of all four C-Sections gives a final expected radon level, inside the Demonstrator, of:

$$A = 41.3 \pm 4.7 mBq = 2.7 \pm 0.31 mBq/m^3 \tag{10.2}$$

By replacing the Demonstrator tracking gas continuously at a flow rate of $2m^3$ per hour this radon activity can be further suppressed by a factor 18.4. Therefore, the radon activity within the tracking gas would be less than the target level of 0.15 mBq/m^3.

In the quest for ever more radio-pure detectors, a new germanium facility, BUGS, has been established at Boulby Underground Laboratory. There are currently four detectors including; a coaxial detector, well detector, BEGe detector and a pre screening BEGe at the BUGS. Together they are able to perform a large and diverse range of measurements from low energy measurements with the BEGe detector to small sample measurements with high efficiency using the well detector.

An analysis programme has been developed for the processing of germanium data. This analysis was verified using calibration sources of known activities to better than 1%, as well as by comparing to results produced using industry leading analysis software provided by Canberra.

Several steps have been taken to improve detector sensitivity, starting with cleaning of the lead and copper shielding, followed by introducing nitrogen purging and finally designing customised shielding. The number of background counts in the 100-2700 keV range was reduced by almost a factor 4.

Having commissioned the BUGS detectors, simulations were carried out for a potential experimental measurement of the decay of ^{96}Zr to the first excited state, 0^+. This is a process which should be possible to all $\beta\beta$-decay isotopes, however it has only been measured in two, ^{100}Mo and ^{150}Nd. Due to its high phase space and Q-value, ^{96}Zr is the next best candidate for a third observation.

The simulations showed it is possible to achieve a factor 4 improvement on current world leading limits on the decay of ^{96}Zr to its first excited state with the need for a zirconium purification process. The experiment would require a large ultra low background germanium detector, with a crystal mass of more than 3 kg, measuring a 20 kg sample of purified natural zirconium oxide for 2 years, producing an sensitivity of:

$$T_{1/2} = 1.34 \times 10^{21} \text{ yr}$$

The results presented in this thesis show clearly the SuperNEMO Demonstrator is on track to meet its stringent radio-purity requirements for the both tracker gas and the detector components.

At the time of writing this thesis, the assembly of the Demonstrator module is nearly complete. First measurement results will confirm if the challenging radio-purity requirements have been fulfilled. Alongside operation of the Demonstrator, a measurement of ^{96}Zr to excited states can further constrain the NME needed to calculate neutrino mass from the measured $0\nu\beta\beta$ half-life.

Bibliography

[1] D. Griffiths, *Introduction to elementary particles*. WILEY-VCH, 2004.

[2] C. L. Cowan Jr., R. Reines, R. B. Harrison, H. W. Kruse, and A. D. McGuire, *Detection of the Free Neutrino: a Confirmation*, Science **124** (July, 1956) 103–104.

[3] R. Davis and D. S. Harmer, *An Attempt to Observe the 37Cl(,e-)37Ar Reaction Induced by Reactor Antineutrinos*, Bull. Am. Phys. Soc. **4** (1959) no. 217, .

[4] E. J. Konopinski and H. M. Mahmoud, *The Universal Fermi Interaction*, Phys. Rev. **92** (Nov, 1953) 1045–1049. http://link.aps.org/doi/10.1103/PhysRev.92.1045.

[5] G. Danby, J. Gaillard, K. A. Goulianos, L. Lederman, N. B. Mistry, et al., *Observation of High-Energy Neutrino Reactions and the Existence of Two Kinds of Neutrinos*, Phys.Rev.Lett. **9** (1962) 36–44.

[6] DONUT Collaboration, K. Kodama et al., *Observation of tau neutrino interactions*, Phys.Lett. **B504** (2001) 218–224, arXiv:hep-ex/0012035 [hep-ex].

[7] e. a. B. Adeva, *Measurement of Z0 decays to hadrons, and a precise determination of the number of neutrino species*, Physics Letters B **237** (March, 1990) 136–146.

[8] ALEPH Collaboration, DELPHI Collaboration, L3 Collaboration, OPAL Collaboration, SLD Collaboration, LEP Electroweak Working Group, SLD Electroweak Group, SLD Heavy Flavour Group, S. Schael et al., *Precision electroweak measurements on the Z resonance*, Phys.Rept. **427** (2006) 257–454, arXiv:hep-ex/0509008 [hep-ex].

[9] K. Eguchi, S. Enomoto, et al., *First Results from KamLAND: Evidence for Reactor Antineutrino Disappearance*, Phys. Rev. Lett. **90** (2003) 021802.

[10] B. Pontecorvo, *Mesonium and anti-mesonium*, Sov.Phys.JETP **6** (1957) 429.

[11] B. Pontecorvo, *Inverse beta processes and nonconservation of lepton charge*, Sov.Phys.JETP **7** (1958) 172–173.

[12] B. Kayser, *Neutrino physics*, eConf **C040802** (2004) L004, `arXiv:hep-ph/0506165 [hep-ph]`.

[13] E. Majorana, *Theory of the Symmetry of Electrons and Positrons*, Nuovo Cim. **14** (1937) 171–184.

[14] M. Goeppert-Mayer, *Double Beta-Disintergration*, Phys. Rev. **48** (1935) no. 6, 512–516.

[15] M. G. Inghram and J. H. Reynolds, *Double Beta-Decay of* Te^{130}, Phys. Rev. **78** (1950) 822–823. `http://link.aps.org/doi/10.1103/PhysRev.78.822.2`.

[16] W. H. Furry, *On Transition Probabilities in Double Beta-Disintergration*, Phys. Rev. **56** (1939) no. 12, 1184–1193.

[17] S. M. Bilenky, S. Pascoli, and S. T. Petcov, *Majorana neutrinos, neutrino mass spectrum,* CP *violation, and neutrinoless double* β *decay: The three-neutrino mixing case*, Phys. Rev. D **64** (2001) 053010.

[18] F. T. Avignone, S. R. Elliott, and J. Engel, *Double beta decay, Majorana neutrinos, and neutrino mass*, Rev. Mod. Phys. **80** (2008) 481–516. `http://link.aps.org/doi/10.1103/RevModPhys.80.481`.

[19] J. Vergados, H. Ejiri, and F. Simkovic, *Theory of Neutrinoless Double Beta Decay*, Rept.Prog.Phys. **75** (2012) 106301, `arXiv:1205.0649 [hep-ph]`.

[20] Particle Data Group, J. Beringer et al., *Review of Particle Physics (RPP)*, Phys.Rev. **D86** (2012) 010001.

[21] Troitsk Collaboration, V. Aseev et al., *An upper limit on electron antineutrino mass from Troitsk experiment*, Phys.Rev. **D84** (2011) 112003, `arXiv:1108.5034 [hep-ex]`.

[22] C. Kraus, B. Bornschein, L. Bornschein, J. Bonn, B. Flatt, et al., *Final results from phase II of the Mainz neutrino mass search in tritium beta decay*, Eur.Phys.J. **C40** (2005) 447–468, arXiv:hep-ex/0412056 [hep-ex].

[23] T. Bowles and R. Robertson, *Tritium beta decay and the search for neutrino mass*, Los Alamos Sci. **25** (1997) 86–91.

[24] G. Drexlin, V. Hannen, S. Mertens, and C. Weinheimer, *Current direct neutrino mass experiments*, Adv.High Energy Phys. **2013** (2013) 293986, arXiv:1307.0101 [physics.ins-det].

[25] P. Bhupal Dev, S. Goswami, M. Mitra, and W. Rodejohann, *Constraining Neutrino Mass from Neutrinoless Double Beta Decay*, arXiv:1305.0056 [hep-ph].

[26] S. A. Thomas, F. B. Abdalla, and O. Lahav, *Upper Bound of 0.28 eV on the Neutrino Masses from the Largest Photometric Redshift Survey*, Phys.Rev.Lett. **105** (2010) 031301, arXiv:0911.5291 [astro-ph.CO].

[27] WMAP Collaboration, G. Hinshaw et al., *Nine-Year Wilkinson Microwave Anisotropy Probe (WMAP) Observations: Cosmological Parameter Results*, arXiv:1212.5226 [astro-ph.CO].

[28] W. Rodejohann, *Neutrinoless double beta decay and neutrino physics*, J.Phys. **G39** (2012) 124008, arXiv:1206.2560 [hep-ph].

[29] T. Ohlsson, H. Zhang, and S. Zhou, *Probing the leptonic Dirac CP-violating phase in neutrino oscillation experiments*, Phys.Rev. **D87** (2013) 053006, arXiv:1301.4333 [hep-ph].

[30] F. T. Avignone, S. R. Elliott, and J. Engel, *Double Beta Decay, Majorana Neutrinos, and Neutrino Mass*, Rev.Mod.Phys. **80** (2008) 481–516, arXiv:0708.1033 [nucl-ex].

[31] J. R. Wilson, *Non-accelerator Neutrino Physics*, IoP HEPP & APP Group Meeting, 2013.

[32] KamLAND-Zen Collaboration, A. Gando et al., *Limit on $0\nu\beta\beta$ Decay of ^{136}Xe from the First Phase of KamLAND-Zen and Comparison with the Positive*

Claim in ^{76}*Ge*, Phys.Rev.Lett. **110** (2013) no. 6, 062502, arXiv:1211.3863 [hep-ex].

[33] KamLAND-Zen Collaboration, A. Gando et al., *Limits on Majoron-emitting double-beta decays of* ^{136}*Xe in the KamLAND-Zen experiment*, Phys.Rev. **C86** (2012) 021601, arXiv:1205.6372 [hep-ex].

[34] KamLand-Zen Collaboration, J. Shirai, *KamLAND-Zen: Status and Future*, Nucl.Phys.Proc.Suppl. **237-238** (2013) 28–30.

[35] S. Umehara, T. Kishimoto, I. Ogawa, R. Hazama, H. Miyawaki, et al., *Neutrino-less double-beta decay of* ^{48}*Ca studied by* CaF_2*(Eu) scintillators*, Phys.Rev. **C78** (2008) 058501, arXiv:0810.4746 [nucl-ex].

[36] S. Umehara, T. Kishimoto, M. Nomachi, S. Yoshida, K. Matsuoka, et al., *Search for neutrino-less double beta decay with CANDLES*, AIP Conf.Proc. **1441** (2012) 448–450.

[37] E. Andreotti, C. Arnaboldi, F. Avignone, M. Balata, I. Bandac, et al., ^{130}*Te Neutrinoless Double-Beta Decay with CUORICINO*, Astropart.Phys. **34** (2011) 822–831, arXiv:1012.3266 [nucl-ex].

[38] CUORE, L. Pattavina, *Status of the CUORE experiment*, J.Phys.Conf.Ser. **447** (2013) 012066.

[39] H. Klapdor-Kleingrothaus, A. Dietz, L. Baudis, G. Heusser, I. Krivosheina, et al., *Latest results from the Heidelberg-Moscow double beta decay experiment*, Eur.Phys.J. **A12** (2001) 147–154, arXiv:hep-ph/0103062 [hep-ph].

[40] H. Klapdor-Kleingrothaus, I. Krivosheina, A. Dietz, and O. Chkvorets, *Search for neutrinoless double beta decay with enriched* ^{76}*Ge in Gran Sasso 1990-2003*, Phys.Lett. **B586** (2004) 198–212, arXiv:hep-ph/0404088 [hep-ph].

[41] C. Aalseth, I. Avignone, F.T., A. Barabash, F. Boehm, R. Brodzinski, et al., *Comment on 'Evidence for neutrinoless double beta decay'*, Mod.Phys.Lett. **A17** (2002) 1475–1478, arXiv:hep-ex/0202018 [hep-ex].

[42] C. Aalseth, F. Avignone, R. Brodzinski, W. Hensley, H. Miley, et al., *Recent results of the IGEX* ^{76}*Ge double-beta decay experiment*, Phys.Atom.Nucl. **63** (2000) 1225–1228.

[43] GERDA Collaboration, M. Agostini et al., *Results on neutrinoless double beta decay of ^{76}Ge from GERDA Phase I*, `arXiv:1307.4720 [nucl-ex]`.

[44] GERDA Collaboration, K. Knöpfle, *GERDA - Status and Perspectives*, Nucl.Phys.Proc.Suppl. **237-238** (2013) 31–33.

[45] Majorana Collaboration, N. Abgrall et al., *The Majorana Demonstrator Neutrinoless Double-Beta Decay Experiment*, `arXiv:1308.1633 [physics.ins-det]`.

[46] GERDA Collaboration, M. Barnabe Heider, *Semiconductor-based experiments for neutrinoless double beta decay search*, Nucl.Phys.Proc.Suppl. **229-232** (2012) 141–145.

[47] J. R. Wilson, *Double beta decay measurement with COBRA*, Nucl.Phys.Proc.Suppl. **221** (2011) 313–316.

[48] R. Saakyan, *Tracking-based Experiments in Double Beta Decay*, Nucl.Phys.Proc.Suppl. **229-232** (2012) 135–140.

[49] R. Saakyan, *Tracking-based Experiment in Double Beta Decay*, Nuclear Physics B Proceedings Supplement **00** (2011) 1–6.

[50] R. A. et al., *Probing New Physics Models of Neutrinoless Double Beta Decay with SuperNEMO*, Eur. Phys. J. **70** (2010) 927–943.

[51] SuperNEMO Collaboration, H. Gómez, *BiPo: A dedicated radiopurity detector for the SuperNEMO experiment*, AIP Conference Proceedings **1549** (2013) no. 1, 94–97.

[52] V. Vasiliev, *Radon in SuperNEMO*, Internal Note **DocDB:297** (2008) .

[53] E. Choi, M. Komori, K. Takahisa, N. Kudomi, K. Kume, K. Hayashi, S. Yoshida, H. Ohsumi, H. Ejiri, T. Kishimoto, K. Matsuoka, and S. Tasaka, *Highly sensitive radon monitor and radon emanation rates for detector components*, Nucl.Instrum.Meth. **A459** (2001) 177–181.

[54] C. Mitsuda, T. Kajita, K. Miyano, S. Moriyama, M. Nakahata, et al., *Development of super-high sensitivity radon detector for the Super-Kamiokande detector*, Nucl.Instrum.Meth. **A497** (2003) 414–428.

[55] E. Wellisch, *The distribution of the active deposit of radium in an electric field*, Philosophical Magazine Series 6 **26** (1913) no. 154, 623–635.

[56] P. Pagelkopf and J. Porstendörfer, *Neutralisation rate and the fraction of the positive ^{218}Po-clusters in air*, Atmospheric Environment **37** (2003) no. 8, 1057 – 1064.

[57] B. N. Laboratory, *National Nuclear Data Center*, http://www.nndc.bnl.gov/nudat2/ .

[58] G. Knoll, *Radiation Detection and Measurement*, ISBN-9780470131480 (2000) .

[59] G. Heusser, W. Rau, B. Freudiger, M. Laubenstein, M. Balata, and T. Kirsten, *^{222}Rn detection at the $\mu Bq/m^3$ range in nitrogen gas and a new Rn purification technique for liquid nitrogen*, Applied Radiation and Isotopes **52** (2000) no. 3, 691 – 695.

[60] J. E. Mott, *Search for double beta decay of ^{82}Se with the NEMO-3 detector and development of apparatus for low-level radon measurements for the SuperNEMO experiment.* PhD thesis, University College London, September, 2013.

[61] J. Busto, *Design of a Preliminary Anti-Radon System*, Presentation doc-3117, CPPM / Universite Aix-Marseille, February, 2014.

[62] J. E. Mott, *First radon measurements of C0*, Technical Report doc-2957, University College London, October, 2013.

[63] H. M. Araújo, J. Blockley, C. Bungau, M. J. Carson, H. Chagani, et al., *Measurements of neutrons produced by high-energy muons at the Boulby Underground Laboratory*, Astroparticle Physics **29** (2008) no. 6, 471–481.

[64] IAEA, *IAEA-385 , Irish Sea Sediment*, https://nucleus.iaea.org/rpst/referenceproducts/referencematerials/radionuclides/IAEA-385.htm
.

[65] CERN, *Platform for the simulation of the passage of particles through matter using Monte Carlo methods*, http://geant4.cern.ch .

[66] CERN, *An object oriented framework for large scale data analysis.*, http://root.cern.ch/drupal/ **Version 5.26** .

[67] U. dark matter collaboration, *UK DM project: radioactivity test results*, http://hepwww.rl.ac.uk/ukdmc/Radioactivity/useful.html .

[68] J. P. Stewart and D. Groff, *LabSOCS™ vs. source-based gamma-ray detector efficiency comparisons for nuclear power plant geometries*, Paper presented at the 48th Annual Radiobioassay and Radiochemical Measurements Conference (2002) .

[69] D. radon instrumentation, *RAD7 RADON DETECTOR*. DURRIDGE Company, 524 Boston Road, Billerica, MA 01821, revision 7.2.2. ed., 2013.

[70] DURRIDGE, *RAD7 Communications Software*, http://www.durridge.com .

[71] L. Baudis and A. e. a. Ferella, *Gator: a low-background counting facility at the Gran Sasso Underground Laboratory*, Journal of Instrumentation **6** (2012) no. 08, P08010.

[72] G. Heusser, M. Laubenstein, and H. Neder, *Low-level germanium gamma-ray spectrometry at the μBq/kg level and future developments towards higher sensitivity*, in *Radionuclides in the Environment Int. Conf. On Isotopes in Env. Studies*, P. Povinec and J. Sanchez-Cabeza, eds., vol. 8 of *Radioactivity in the Environment*, pp. 495 – 510. Elsevier, 2006. `http://www.sciencedirect.com/science/article/pii/S1569486005080393`.

[73] S. Stoica, *Two-neutrino double-beta decay half-lives of 96Zr and looMo Two-neutrino double-beta decay half-lives of ^{96}Zr and ^{100}Mo to excited states of ^{96}Mo and ^{100}Ru*, Physics Letters B **350** (1995) no. 2, 152–157.

[74] Y. Ren and Z. Ren, *Systematic law for half-lives of double-β decay with two neutrinos*, Physical Review C **89** (2014) no. 6, 064603.

[75] S. W. Finch and W. Tornow, *Search for two-neutrino double-β decay of ^{96}Zr to excited states of ^{96}Mo.*, Physical Review C **92** (2015) no. 4, 045501.

[76] R. Arnolda, C. Augierb, J. Bakerc, A. Barabashd, O. Binga, D. Blumb, et al., *Chemical purification of molybdenum samples for the NEMO 3 experiment*, Nuclear Instruments and Methods in Physics Research Section A: Accelerators, Spectrometers, Detectors and Associated Equipment **474** (2001) no. 1, 93–100.